ISAE - Supaero & Politecnico di Torino

Master's thesis in Aerospace Engineering

A.a. 2024-2025

Numerical and Experimental Investigation of Particle-Induced Erosion in Composite Material Components

Advisors:
Prof. Marco Gherlone
Prof. Frédéric Lachaud
Ph.D. Cand. Adrien Sapet

Student:
Giorgio Biggi

Contents

Chapter 1

Context of the study

The basic principle of helicopter flight sustenance relies on the rotation of the rotor, powered by the engine. These two essential components must be reliable, efficient, robust and lightweight, as their performance is intrinsically linked to the potential propagation of cracks within the material used. Wear, defined as the progressive deterioration of a solid surface due to mechanical contact, affects both the turboshaft and the rotor blades, altering their sections and leading to power loss. This wear can significantly reduce helicopter flight time by necessitating earlier and more stringent maintenance inspections. This thesis focuses on developing an optimized numerical model to study the behavior of erosion in composite components caused by multiple particle impingement, specifically focusing on the interaction between sand and blades. The initial phase of the study aims to create an accurate simulation of sand, which forms the foundation for constructing the finite element model. Finally validation of the model is initiated through experimental tests.

1.1 Experimental approach

The experimental purpose is to quantify the erosion rate on samples made of an orthotropic composite structured in 26 layers each one is composed by [0,90] carbon 2x2 twill fibers plunged in a resin expoxy M49. A sample, presented in picture 5.8, measure $140x50$ mm with a depth of 5 mm. All samples are polished before the sand blasting is performed.

Figure 1.1: Sample

Several tests were performed by changing: the angle between the erosive material and the plate, impingment angle, and the duration of wear exposure. As erosive material it is used sand that has a density equal to 2.33 g/mL and a particle size distribution presented in figure 1.2. An in-depth discussion of this part can be found in the dedicated chapter.

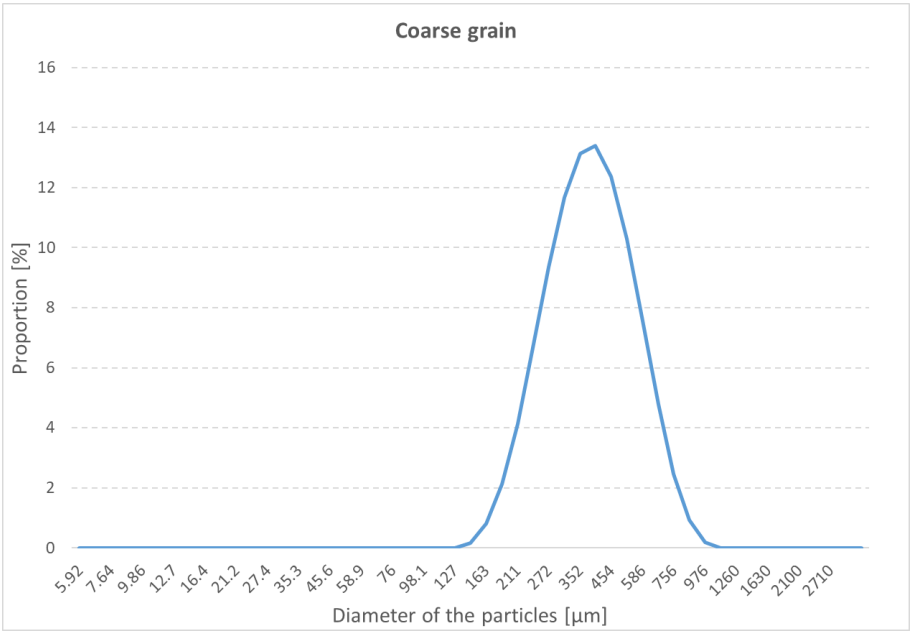

Figure 1.2: Particle size distribution

1.2 Numerical simulation approach

It is intended to simulate the behavior of a composite plate made of the material described above, subjected to erosion caused by the impact of sand particles. For this purpose, a script was initially developed in MATLAB to extract a 3D model of the sand particles to be used in the simulation, in order to reproduce the actual erosion rate as closely as possible. The entire simulation was conducted using Abaqus Explicit software. An in-depth discussion of this part can be found in the dedicated chapter.

Chapter 2

State of art

2.1 Fiber reinforced composite materials

The target of the composite materials is to improve the materials properties using the combination of different constituent. In engineering it is a well-established principle that the combination of two or more materials can result in a composite with more advantageous characteristics, maximizing the positive properties of the components. This principle applies to all types of properties – physical, chemical, and mechanical – while also offering the additional benefit of reduced density and, in some cases, lower costs, factors that are important to engineers utilizing these materials.
Composite materials are categorized based on the type of reinforcement and matrix they contain. In particular, one classification can be obtained looking to the structure of the reinforcement, figure 2.1, where it can be obtaine: particulate composite, flake composite and fiber reinforced [1].

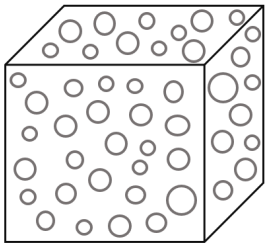

(a) Particulate composite

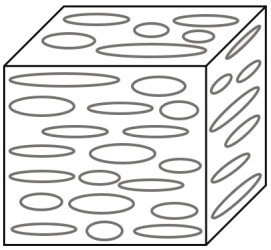

(b) Flake composite

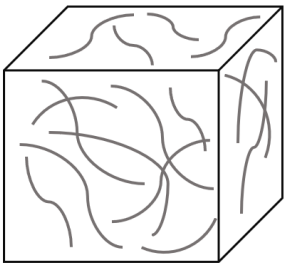

(c) Fiber reinforced composite

Figure 2.1: Types of reinforcement

Fiber-reinforced composites (FRC) consist of fibers embedded in a matrix that holds them in the desired positions and shields them from external environmental factors. When the fibers are all aligned parallel to each other, the resulting composite is referred to as unidirectional (UD). This type of composite is designed in order to achieve that most of the load is applied in the direction of the fibers as they go to absorb it. On the other hand, if the composite material is formed by stacking multiple layers, with orientations designed to account for the directional forces it will experience, the result is a laminate, figure 2.2. The properties of the laminate depends on the direction of the fibers.

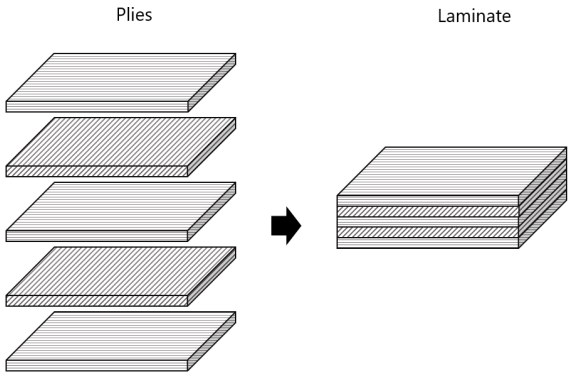

Figure 2.2: Laminate

An important aspect in fiber-reinforced composites is how the fibers are arranged

within the material. The fiber arrangement or weave pattern significantly influences the mechanical properties, flexibility, and manufacturability of the composite. Common fiber weave types include, figure 2.3 [1]:

- Plain weave: fibers are woven in a simple above-below pattern. It is usually used for nonstructural components in aerospace industry;
- Twill weave: obtained by passing fibers over two or more fibers before passing over the others. In fact there are different options, like 2x2 twill means that the tow passes over two tows and then under two tows. This types are used for structural part in aerospace industry;
- Harness stin waves: this type is obtained by passing the fibers over and then under a higher number of fibers than in the previous category; there are several types which are classified according to their flexibility, $4HS$, $5HS$, $8HS$, where the number indicates how many fibers are crossed before the weft passes under another fiber obtaining that higher the number is, the more flexible they turn out to be.

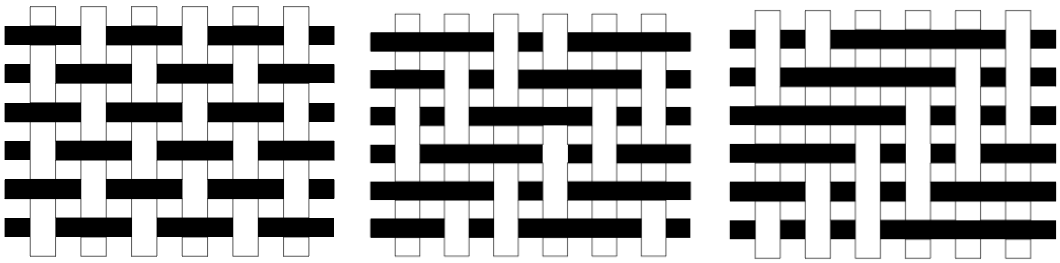

(a) Plain weave (b) 2x2 twill weave (c) $4HS$ wave

Figure 2.3: Fiber wear types

Another classification of composite materials can be made on the basis of the matrix used, which has significantly lower mechanical properties than fibers, but plays a key role since, in addition to the aforementioned functions of acting as an adhesive and protection for the fibers, it has the function of sending stresses from the structure to the fibers. The most common matrix are ceramic matrix, metal matrix and organic matrix.

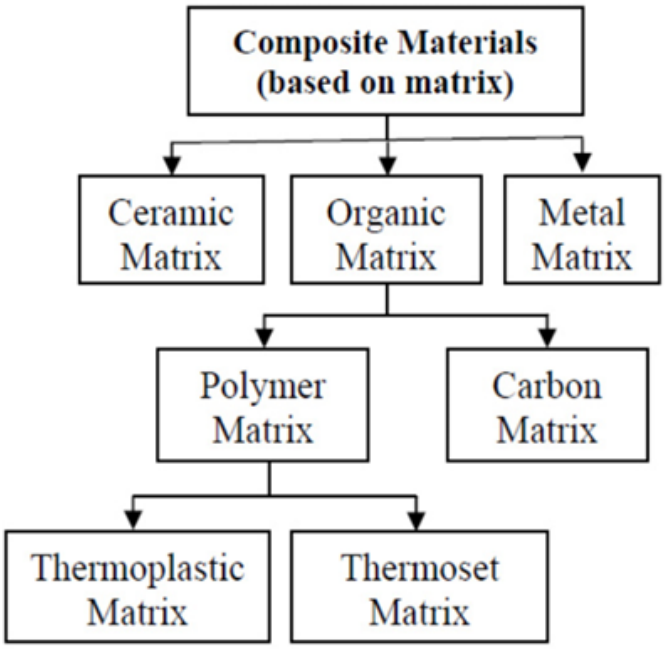

Figure 2.4: Common matrix types[2]

The polymer matrix, that is part of the organic matrix family, is the one that finds the most application in aerospace due to its low weight. This type of matrix can be divide in two groups: thermosets and thermoplastics.
Thermosetting resins occur in a very dense liquid state at room temperature, it irreversibly assumes a solid state the moment it is brought to the curing temperature. It consists of: a saturated base monomer, a crosslinking agent, a diluent, a catalyst and a stabilizer. The action performed by the catalyst, after a certain amount of energy has been administered (thermal, irradiation, etc...), leads to the origin of polymer chains in the three directions, connected by cross-links, thus reaching the solid state. This process leads the matrix to have viscoelastic behavior. The most widely used thermosetting resins are: epoxy, polyimide, polyester, phenolic and silicone. The most popular for the production of high-performance composites turn out to be epoxy resins.
Thermoplastic resins, unlike their predecessors, are in a solid state at room temperature. When they are heated, once they exceed a certain temperature threshold, called the glass transition temperature, they begin to assume a rubbery state that promotes their formability; once cooled they regain their original resistance. This behavior is given by the fact that their micro molecular structure consists of Van der Waals bonds that are brought to rupture with increasing temperature. Thermoplastic resins include polypropylenes, polyamides and polycarbonates [1].

2.2 Orthotropic Material Mechanics

Hooke's law, which describes the elastic behavior of a material, in three dimensions is expressed by the equation 2.1 [3].

$$\sigma_{ij} = C_{ijkl}\varepsilon_{kl} \tag{2.1}$$

Since the stress and strain tensors are symmetric, the stiffness tensor C, which has 36 independent elements, can be represented as a 6x6 matrix. It can be express using the Voigt notation, equation 2.2, that is for an anisotropic material.

$$\begin{Bmatrix} \sigma_{11} \\ \sigma_{22} \\ \sigma_{33} \\ \sigma_{12} \\ \sigma_{13} \\ \sigma_{23} \end{Bmatrix} = \begin{bmatrix} C_{11} & C_{12} & C_{13} & C_{14} & C_{15} & C_{16} \\ C_{21} & C_{22} & C_{23} & C_{24} & C_{25} & C_{26} \\ C_{31} & C_{32} & C_{33} & C_{34} & C_{35} & C_{36} \\ C_{41} & C_{42} & C_{43} & C_{44} & C_{45} & C_{46} \\ C_{51} & C_{52} & C_{53} & C_{54} & C_{55} & C_{56} \\ C_{61} & C_{62} & C_{63} & C_{64} & C_{65} & C_{66} \end{bmatrix} \begin{Bmatrix} \varepsilon_{11} \\ \varepsilon_{22} \\ \varepsilon_{33} \\ \gamma_{12} \\ \gamma_{13} \\ \gamma_{23} \end{Bmatrix} \tag{2.2}$$

An orthotropic material has three planes of symmetry that coincide with the coordinate planes. With this type of material the stiffness matrix contains only nine elements, equation 2.3.

$$\begin{Bmatrix} \sigma_{11} \\ \sigma_{22} \\ \sigma_{33} \\ \sigma_{12} \\ \sigma_{13} \\ \sigma_{23} \end{Bmatrix} = \begin{bmatrix} C_{11} & C_{12} & C_{13} & 0 & 0 & 0 \\ C_{12} & C_{22} & C_{23} & 0 & 0 & 0 \\ C_{13} & C_{23} & C_{33} & 0 & 0 & 0 \\ 0 & 0 & 0 & C_{44} & 0 & 0 \\ 0 & 0 & 0 & 0 & C_{55} & 0 \\ 0 & 0 & 0 & 0 & 0 & C_{66} \end{bmatrix} \begin{Bmatrix} \varepsilon_{11} \\ \varepsilon_{22} \\ \varepsilon_{33} \\ \gamma_{12} \\ \gamma_{13} \\ \gamma_{23} \end{Bmatrix} \tag{2.3}$$

Where $C_{ij} = C_{ji}$.
This equation is used to study unidirectional fiber-reinforced composite materials (UD), where the elastic behavior varies along the principal directions due to the fiber orientation. Substituting with the properties of the ply is obtained the equation 2.4.

$$\begin{Bmatrix} \sigma_{11} \\ \sigma_{22} \\ \sigma_{33} \\ \sigma_{12} \\ \sigma_{13} \\ \sigma_{23} \end{Bmatrix} = \begin{bmatrix} \frac{1-\nu_{23}\nu_{32}}{E_2E_3\Delta} & \frac{\nu_{21}+\nu_{31}\nu_{23}}{E_2E_3\Delta} & \frac{\nu_{31}+\nu_{21}\nu_{32}}{E_2E_3\Delta} & 0 & 0 & 0 \\ \frac{\nu_{12}+\nu_{13}\nu_{32}}{E_1E_3\Delta} & \frac{1-\nu_{31}\nu_{13}}{E_1E_3\Delta} & \frac{\nu_{32}+\nu_{31}\nu_{12}}{E_1E_3\Delta} & 0 & 0 & 0 \\ \frac{\nu_{13}+\nu_{12}\nu_{23}}{E_1E_2\Delta} & \frac{\nu_{23}+\nu_{13}\nu_{21}}{E_1E_2\Delta} & \frac{1-\nu_{12}\nu_{21}}{E_1E_2\Delta} & 0 & 0 & 0 \\ 0 & 0 & 0 & G_{12} & 0 & 0 \\ 0 & 0 & 0 & 0 & G_{13} & 0 \\ 0 & 0 & 0 & 0 & 0 & G_{23} \end{bmatrix} \begin{Bmatrix} \varepsilon_{11} \\ \varepsilon_{22} \\ \varepsilon_{33} \\ \gamma_{12} \\ \gamma_{13} \\ \gamma_{23} \end{Bmatrix} \tag{2.4}$$

$$\Delta = \frac{1 - \nu_{12}\nu_{21} - \nu_{23}\nu_{32} - \nu_{13}\nu_{31} - 2\nu_{12}\nu_{23}\nu_{31}}{E_1E_2E_3} \tag{2.5}$$

Where:

- E_i and G_{ij} are the Young and shear moduli;
- ν_{ij} are the Poisson ratios.

Due to the symmetry of the stiffness matrix, the following relations can be made.

$$\frac{\nu_{21} + \nu_{31}\nu_{23}}{E_2E_3\Delta} = \frac{\nu_{12} + \nu_{13}\nu_{32}}{E_3E_1\Delta} \tag{2.6}$$

$$\frac{\nu_{31} + \nu_{21}\nu_{32}}{E_2E_3\Delta} = \frac{\nu_{13} + \nu_{12}\nu_{23}}{E_1E_2\Delta} \tag{2.7}$$

$$\frac{\nu_{32} + \nu_{31}\nu_{12}}{E_3E_1\Delta} = \frac{\nu_{23} + \nu_{13}\nu_{21}}{E_1E_2\Delta} \tag{2.8}$$

Inverting the stiffness matrix yields the compliance matrix that describes how much a material deforms under the action of a stress. For a orthotropic material is espressed in equation 2.9 [3].

$$\begin{Bmatrix} \varepsilon_{11} \\ \varepsilon_{22} \\ \varepsilon_{33} \\ \gamma_{12} \\ \gamma_{13} \\ \gamma_{23} \end{Bmatrix} = \begin{bmatrix} \frac{1}{E_1} & -\frac{\nu_{21}}{E_2} & -\frac{\nu_{31}}{E_3} & 0 & 0 & 0 \\ -\frac{\nu_{12}}{E_1} & \frac{1}{E_2} & -\frac{\nu_{32}}{E_3} & 0 & 0 & 0 \\ -\frac{\nu_{13}}{E_1} & -\frac{\nu_{23}}{E_2} & \frac{1}{E_3} & 0 & 0 & 0 \\ 0 & 0 & 0 & \frac{1}{G_{12}} & 0 & 0 \\ 0 & 0 & 0 & 0 & \frac{1}{G_{13}} & 0 \\ 0 & 0 & 0 & 0 & 0 & \frac{1}{G_{23}} \end{bmatrix} \begin{Bmatrix} \sigma_{11} \\ \sigma_{22} \\ \sigma_{33} \\ \sigma_{12} \\ \sigma_{13} \\ \sigma_{23} \end{Bmatrix} \tag{2.9}$$

Where

$$\frac{\nu_{ij}}{E_i} = \frac{\nu_{ji}}{E_j} \tag{2.10}$$

2.3 Laminated plate theory

For the study of laminated composite materials, laminated plate theory is used, which is based on Kirchoff-Love hypothesis, which assume that the plate cross sections, normal to the mean surface before deformation, remain linear, normal to the mean surface and do not experience elongation after deformation;
These assumptions imply that the transverse normal strain ε_{zz} and transverse shear strains, γ_{xz} γ_{yz}, are equal to zero; also, transverse normal displacement is independent of the transverse (or thickness) coordinate.
The displacements trend is reported in equation 2.11 [4].

$$\begin{cases} u_x(x,y,z) = u_x^0(x,y) + z\,\Phi_x(x,y) \\ u_y(x,y,z) = u_y^0(x,y) + z\,\Phi_y(x,y) \\ u_z(x,y,z) = u_z^0(x,y) \end{cases} \tag{2.11}$$

Where the peak 0 denotes the value in the middle plane of the plate.
From the assumption that ε_{zz} is zero, it follows that:

$$\varepsilon_{zz} = \frac{\partial u_z}{\partial z} = 0 \Rightarrow u_z^0(x,y) = \text{const.} \tag{2.12}$$

this implies that the transverse displacement u_z is constant along z and the normal does not shorten. In the analysis of problems involving thin plates and shells, plane stress assumptions are often used, since these problems are typically related to thin surfaces. However, plane strain is more common in beam theory, where some out-of-plane deformation is assumed to be zero. In many equivalent single-layer theories, a contradiction is introduced by inconsistently applying both assumptions about strain fields. This leads to a phenomenon known as locking mechanism, which can make the plate or shell model not applicable in some cases. In particular, thickness locking (or Poisson locking) occurs, which hinders proper deformation through the thickness of the structure. Thickness locking (TL) prevents that, in single equivalent layer analysis, normal displacement through thickness (constant or linear) leads to a three-dimensional solution in thin plate problems. This implies that the transverse normal strain is zero or constant.
A well-known technique to counteract thickness locking is to change the elastic

stiffness coefficients. This is done by imposing the "contradictory" condition in which the transverse normal stress σ_{zz} is zero. This modification helps to reduce the blocking effect and allows for a more accurate solution.

From the assumption ($\gamma_{xz} = 0$) ensues

$$\frac{\partial u}{\partial z} + \frac{\partial w}{\partial x} = 0 \quad \Rightarrow \quad u_{,z} + w_{,x} = 0 \tag{2.13}$$

By substituting the expressions of u and v is obtained:

$$\frac{\partial \left(u^0(x,y) + z\Phi_x(x,y)\right)}{\partial z} + \frac{\partial w^0(x,y)}{\partial x} = 0 \tag{2.14}$$

$$\frac{\partial u^0(x,y)}{\partial z} + \Phi_x(x,y) + \frac{\partial w^0(x,y)}{\partial x} = 0 \tag{2.15}$$

$$\Phi_x(x,y) + w^0_{,x}(x,y) = 0 \quad \Rightarrow \quad \Phi_x(x,y) = -w^0_{,x}(x,y) \tag{2.16}$$

It is the same process imposing the other ipothesis $\gamma_{yz} = 0$:

$$v_{,z} + w_{,y} = 0 \quad \Rightarrow \quad \Phi_y(x,y) = -w^0_{,y}(x,y) \tag{2.17}$$

The displacement field of Kirchoff's theory is reported in Eq. 2.18.

$$\begin{cases} u(x,y,z) = u^0(x,y) - zw^0_{,x}(x,y) \\ v(x,y,z) = v^0(x,y) - zw^0_{,y}(x,y) \\ w(x,y,z) = w^0(x,y) \end{cases} \tag{2.18}$$

Reporting non-zero deformations 2.19

$$\begin{cases} \varepsilon_{xx} = \frac{\partial u}{\partial x} = u_{,x} = (u^0 - zw^0_{,x})_{,x} = u^0_{,x} - zw^0_{,xx} \\ \varepsilon_{yy} = \frac{\partial v}{\partial y} = v_{,y} = (v^0 - zw^0_{,y})_{,y} = v^0_{,y} - zw^0_{,yy} \\ \gamma_{xy} = \frac{\partial u}{\partial y} + \frac{\partial v}{\partial x} = u_{,y} + v_{,x} = (u^0 - zw^0_{,x})_{,y} + (v^0 - zw^0_{,y})_{,x} = u^0_{,y} + v^0_{,x} - 2zw^0_{,xy} \end{cases} \tag{2.19}$$

They can be rewrite in Eq.2.20

$$\begin{cases} \varepsilon_{xx} = \varepsilon^0_{xx} + zk_{xx} \\ \varepsilon_{yy} = \varepsilon^0_{yy} + zk_{yy} \\ \gamma_{yx} = \gamma^0_{yx} + zk_{xy} \end{cases} \tag{2.20}$$

Where the apex 0 indicates the membranal deformations in the middle plane of the plate, and the curves are k_{ij}:

$$k_{xx} = -w_{,xx} \quad ; \quad k_{yy} = -w_{,yy} \quad ; \quad k_{xy} = -2w_{,xy} \tag{2.21}$$

In particular, k_{xy} represents the torsional component.

The stresses and moments per unit length, associated with the stresses σ_{xx}, σ_{yy} and τ_{xy}, are determined by integrating them along the thickness of the plate [4].

$$N_{xx}(x,y) = \int_{-h/2}^{h/2} \sigma_{xx}\, dz; \quad N_{yy}(x,y) = \int_{-h/2}^{h/2} \sigma_{yy}\, dz; \quad N_{xy}(x,y) = \int_{-h/2}^{h/2} \tau_{xy}\, dz \tag{2.22}$$

$$M_{xx}(x,y) = \int_{-h/2}^{h/2} \sigma_{xx}\, z\, dz; \quad M_{yy}(x,y) = \int_{-h/2}^{h/2} \sigma_{yy}\, z\, dz; \quad M_{xy}(x,y) = \int_{-h/2}^{h/2} \tau_{xy}\, z\, dz \tag{2.23}$$

Rewriting Hooke's law in the context of classical lamination theory (CLT) and considering an orthotropic material, equation 2.2 becomes:

$$\begin{Bmatrix} \sigma_{xx} \\ \sigma_{yy} \\ \sigma_{xy} \end{Bmatrix} = \begin{bmatrix} \bar{C}_{11} & \bar{C}_{12} & 0 \\ \bar{C}_{12} & \bar{C}_{22} & 0 \\ 0 & 0 & \bar{C}_{66} \end{bmatrix} \begin{Bmatrix} \varepsilon_{xx} \\ \varepsilon_{yy} \\ \varepsilon_{xy} \end{Bmatrix} \tag{2.24}$$

Where:

$$\bar{C}_{11} = C_{11} - \frac{C_{13}^2}{C_{33}} \quad \bar{C}_{12} = C_{12} - \frac{C_{13}C_{23}}{C_{33}} \quad \bar{C}_{22} = C_{22} - \frac{C_{23}^2}{C_{33}} \quad \bar{C}_{66} = C_{66} \tag{2.25}$$

Substituting equation 2.24 into equations 2.22 and 2.23, is obtained:

$$\begin{Bmatrix} N_x \\ N_y \\ N_{xy} \\ M_x \\ M_y \\ M_{xy} \end{Bmatrix} = \begin{bmatrix} A_{11} & A_{12} & A_{14} & B_{11} & B_{12} & B_{14} \\ A_{21} & A_{22} & A_{24} & B_{12} & B_{22} & B_{24} \\ A_{14} & C_{24} & C_{44} & B_{14} & B_{24} & B_{44} \\ B_{11} & B_{12} & B_{14} & D_{11} & D_{12} & D_{14} \\ B_{12} & B_{22} & B_{24} & D_{12} & D_{22} & D_{24} \\ B_{14} & B_{24} & B_{44} & D_{14} & D_{24} & D_{44} \end{bmatrix} \begin{Bmatrix} \varepsilon_{xx}^0 \\ \varepsilon_{yy}^0 \\ \varepsilon_{xy}^0 \\ \kappa_x \\ \kappa_y \\ \kappa_{xy} \end{Bmatrix} \tag{2.26}$$

In which A_{ij}, B_{ij} and C_{ij} are calculated with the equations:

$$(A_{ij}, B_{ij}, D_{ij}) = \int_{-h/2}^{h/2} \bar{C}_{ij}(1, z, z^2)\, dz = \sum_{k=1}^{N} \int_{z_k}^{z_{k+1}} \bar{C}_{ij}^{(k)}(1, z, z^2)\, dz \tag{2.27}$$

where N represents the number of layers forming the composite and k denotes the considered layer. A, B, and D matrices are the stiffness matrices that relate the membrane forces and bending moments to the strains and curvatures in laminate theory:

- A_{ij} is the extensional stiffness;
- B_{ij} is the bending-extensional coupling stiffness. If $B_{ij} \neq 0$, it means that a state of stress also generates curvature and vice versa, which occurs in asymmetric laminates;
- D_{ij} is the bending stiffness.

2.4 Damage mechanisms

Damage refers to a set of irreversible changes in a material caused by physical or chemical processes resulting from the application of thermomechanical loads [5]. In this section are reported the principal damage mechanisms observed in composite materials.

2.5 Fiber breakage

When a unidirectional composite is subjected to tensile loading along the fiber direction, the fibers bear the majority of the load. As the load increases, fibers begin to fail at their weakest points, leading to stress redistribution between the fibers and the matrix, figure 2.5. The fiber breakage process is inherently statistical, as fiber strength varies along the length of the fibers and between individual fibers. Consequently, the longitudinal tensile strength of the composite is challenging to predict and depends on both the matrix properties and the effectiveness of the fiber-matrix interface bonding[5].

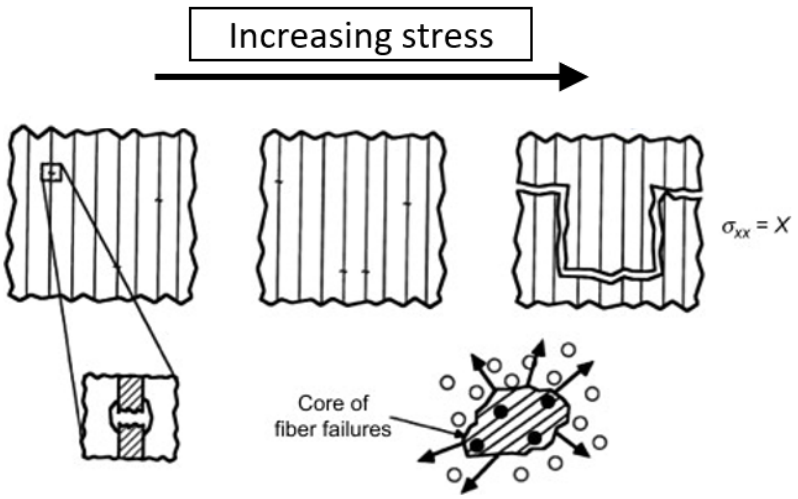

Figure 2.5: Increasing stress during fiber breakage[5]

2.5.1 Matrix micro-cracking

Matrix microcracking, also known as intralaminar cracking, refers to the formation of cracks parallel to the fiber direction within the ply. These cracks typically occur when the material is subjected to transverse loading or as a result of fatigue and thermal stresses, figure 2.6. They often originate from fiber-matrix debonding or manufacturing defects. This type of damage is usually the first to appear in such materials. This is because the mechanical properties of the composite in the direction transverse to the fibers primarily depend on the matrix, which generally exhibits lower strength and stiffness compared to the fibers. Matrix microcracking leads to a reduction in material stiffness and can trigger other damage mechanisms, such as delamination or fiber breakage[6].

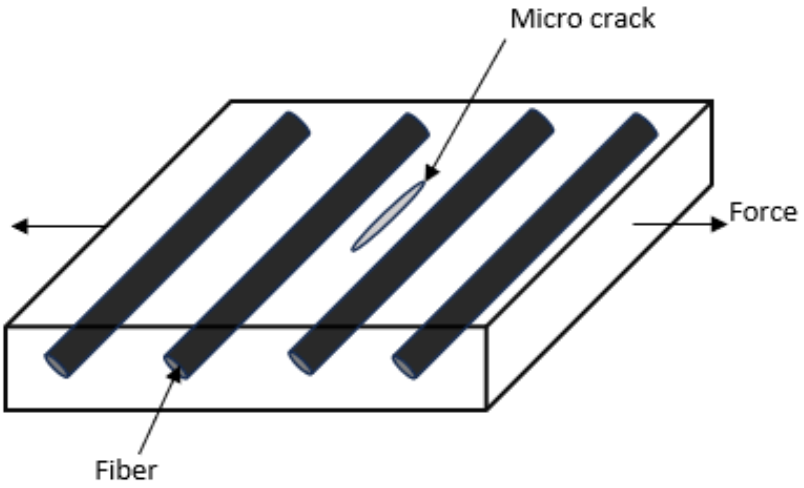

Figure 2.6: Schematic representation of matrix micro-cracking

2.5.2 Interfacial debonding

Interfacial debonding, also known as fiber-matrix debonding, refers to the separation of fibers from the surrounding matrix. The properties of the fiber-matrix interface significantly influence the overall performance of the composite, playing a crucial role in stress transfer[5].
As the load on the composite increases, the fibers and the matrix deform differently. When the deformation reaches a critical level, the resulting stresses lead to the separation of the fibers from the matrix along the interface, figure 2.7.

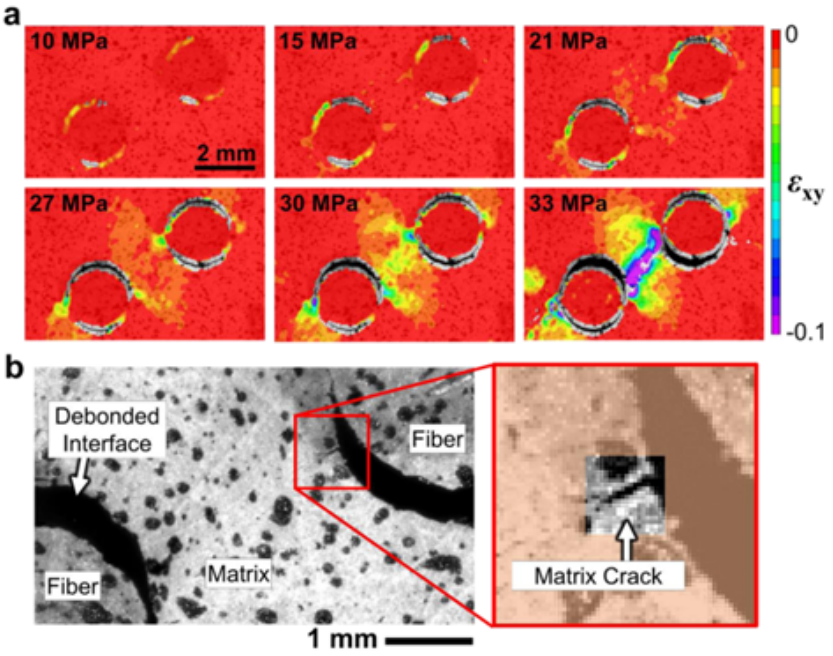

Figure 2.7: Fiber-matrix debond[7]

2.5.3 Delamination

Delamination, also known as interlaminar cracking, refers to the separation of two adjacent plies in a laminate. This type of damage is a critical issue for fiber-reinforced composite materials due to their low interlaminar strength. Delamination is the main failure mode observed when a compressive load is applied [8].
Delamination can occur near a through-the-thickness exposed surface, such as a cut edge. When the material is loaded in this region, through-the-thickness normal and shear stresses develop, leading to the separation of the plies. Additionally, delamination can result from impacts on the laminate, a phenomenon commonly observed in thermoset composites.
Moreover, interlaminar cracks can arise as a consequence of previous intralaminar cracking. The growth of interlaminar cracks is influenced by the interlaminar fracture toughness of the matrix, which plays a crucial role in determining the material's resistance to delamination[5].

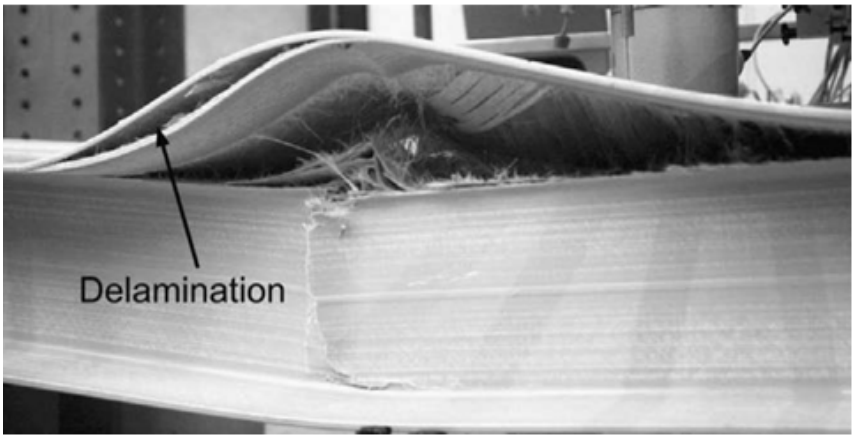

Figure 2.8: Separation of compressed face layer from web and subsequent delamination in face layer of FRP bridge deck [9]

2.5.4 Microbuckling

The phenomenon of microbuckling can occur when a composite is subjected to compression. It consists of the decohesion of the fibres of the face subjected to compression. These decohesions are uniformly distributed across the surface and propagate in a stable manner. Their wavelengths are initially on the order of half the thickness. This phenomenon is noted only in the case of unidirectional specimens and $[0/90/0/90/0]_s$ laminates[5].

2.6 Erosion mechanisms

Erosion is a wear mechanism caused by the high-speed collision of small particles with the target surface, leading to material removal.
The interaction forces are the primary factors contributing to material failure during the erosion process.
Based on the momentum theorem, the contact forces between the erodent and the

target material can be expressed as follows:

$$F_t = \frac{d(m \cdot v \cdot cos(\alpha))}{dt} \tag{2.28}$$

$$F_n = \frac{d(m \cdot v \cdot sin(\alpha))}{dt} \tag{2.29}$$

where F_t is the tangential contact force, F_n is the normal contact force, m is the mass of the erodent, v is the impact velocity and α is the impact angle.
Two basic mechanisms for erosion, namely shear erosion and deformation erosion (ploughing erosion).
In shear erosion, which occurs at low impact angles, the particle cuts away a portion of material, forming raised edges along the sides of the shear zone. This behavior is due to the fact that, at low impact angles, both the tangential and normal contact forces exhibit multiple peaks and valleys during the dynamic erosion process. This implies that the main erosion mechanisms are plastic deformation and cutting caused by tangential shear.
In deformation erosion, which occurs at high impact angles, material detachment happens through fragmentation with each individual impact. During the dynamic erosion process, the normal force rapidly increases over time and then decreases to zero. Vertical cracking and surface fatigue are the primary erosion mechanisms due to repetitive solid particle collisions [10].

2.6.1 Metallic materials erosion mechanism

In metallic materials, the deformation pattern of the target material due to particle collisions changes dramatically during dynamic erosion. This behavior is due to two important parameters: plastic strain and strain rate.
Numerical approaches offer valuable insights for both the design and performance prediction of structures that absorb significant amounts of energy in a short time frame, such as vehicles and aircraft under impact conditions. However, these approaches rely on a constitutive description of the material's nonlinear dynamic mechanical behavior, typically expressed through constant parameters within suitable analytical models, such as the Cowper–Symonds material model [11], that is used to represent the mechanical behavior of several materials at high strain rates, or Johnson-Cook plasticity model.
In order to define the parameters there are several experimental techniques: quasi-static tensile tests (from 10^{-4} to 1 s^{-1}), split Hopkinson pressure bar (from 10^2 to 10^4 s^{-1}), Taylor test (from 10^4 to 10^6 s^{-1}) and inverse flyer plate (from 10^6 to 10^9 s^{-1}).
The Cowper-Symonds equation [12], is an elasto-plastic model that incorporates both strain hardening and strain rate hardening, where materials increase in strength under plastic deformation. This phenomenon is referred to as work hardening or strain hardening [11]. The Cowper-Symonds equation scales the yield stress (σ_y) by two factors: a strain factor and a strain rate factor as shown in Eq. (2.30).

$$\sigma_y = [1 + (\frac{\dot{\varepsilon}}{C})^{\frac{1}{P}} \cdot (\sigma_0 + \beta E_p \varepsilon_p^{eff})] \tag{2.30}$$

Where:

- σ_0 is the initial yield stress;
- $\dot{\varepsilon}$ is the strain rate;
- C and P are the Cowper–Symonds strain rate parameters;
- β is the strain hardening parameter, which adjust the contribution of isotropic and kinematic hardening;
- ε_p^{eff} is the effective plastic strain;
- E_p is the plastic hardening modulus which is given in terms of the elastic modulus E and the tangent elastic modulus E_{tan}

$$E_p = \frac{E_{tan}E}{E - E_{tan}} \tag{2.31}$$

A model, that consider the Cowper-Symonds equation to modify the yeld stress value, is presented in Eq.(2.32) [10].

$$\frac{\sigma}{\sigma_0} = 1 + \left(\frac{\dot{\varepsilon}}{D_y}\right)^{\frac{1}{q}} \tag{2.32}$$

where:

- σ is the dynamic flow stresses;
- σ_0 is the static flow stresses;
- $\dot{\varepsilon}$ is the strain rate;
- D_y and q are constants of target material.

If a multi-axial stress condition is considered σ and ε correspond to the equivalent dynamic flow stress and the associated equivalent strain rate, respectively.
In an uniaxial stress condition it is considered a modified equation

$$\sigma = \sigma_0 \cdot \left[1 + \left(\frac{(\varepsilon_u - \varepsilon_y)\dot{\varepsilon}}{(\varepsilon - \varepsilon_y)D_u + (\varepsilon_u - \varepsilon)D_y}\right)^{\frac{1}{q}}\right] \tag{2.33}$$

Where:

- ε_y is the yield strain;
- ε_u is the ultimate strain;
- D_y and D_u are the coefficients associated with ε_y and ε_u, respectively;
- D_u is a coefficient evaluated from the strain rate sensitivity properties at the ultimate tensile strength of a material.

Another widely used model is the Johnson-Cook model, which includes strain rate and temperature dependence. The model is described by the equation (2.34) [13].

$$\sigma = [A + B \cdot \varepsilon_p^n][1 + C \cdot ln(\frac{\dot{\epsilon}_p}{\dot{\varepsilon}_0})][1 - (T^*)^m] \tag{2.34}$$

Where:

- σ is the equivalent stress response;
- ε_p and $\dot{\varepsilon}_p$ are the equivalent plastic strain and strain rate, respectively;
- $\dot{\varepsilon}_0$ is a normalizing reference strain rate;
- A and B are the strain hardening parameters;
- C is a dimensionless strain rate hardening coefficient;
- n and m are power exponents of the strain hardening and thermal softening terms.

T^* is a normalized temperature defined as:

$$T^* = \begin{cases} 0; & \text{if } T < T_{\text{transition}} \\ \frac{T - T_{\text{transition}}}{T_{\text{melt}} - T_{\text{transition}}}; & \text{if } T_{\text{transition}} \leq T \leq T_{\text{melt}} \\ 1; & \text{if } T > T_{\text{melt}} \end{cases} \tag{2.35}$$

where T_{melt} is the melting temperature above which the material is fluid and the hardening effect should totally vanish. $T_{transition}$ is a transition temperature at or below which the response is not temperature dependent.

The phenomenon under study involves multiple particle impacts on a specimen, making it necessary to use the tools of fracture mechanics. Additionally, the dynamic nature associated with erosion must be considered. This is summarized in the incubation time fracture criterion, a model that has proven to be effective for dynamic fracture analysis [14], the fracture at time t occurs if the inequality (2.36) holds.

$$\frac{1}{\tau} \int_{t-\tau}^{t} \sigma(s)\, ds \geq \sigma_c \tag{2.36}$$

$\sigma(t)$ is a time-dependent tensile stress, σ_c is the ultimate static tensile stress and τ is microstructural time of brittle fracture or incubation time. The parameter τ defines the material's response to a dynamically applied load and should be considered as independent material constant.
To define the criteria to removal of material it can be considered the combined use of incubation time criterion and Hertz contact theory [14], obtained Eq. (2.37)

$$\frac{1 - 2\nu}{2\pi} \frac{k}{R} \sqrt{h_0} \max_t \int_{t-\tau}^{t} \sqrt{\sin\left(\frac{\pi s}{t_0}\right)}\, ds = \tau \sigma_c \tag{2.37}$$

$$k = \frac{4\sqrt{R}E}{3(1-\nu^2)} \qquad h_0 = \left(\frac{5}{4k}mV^2\right)^{\frac{1}{5}} \qquad t_0 = 2.94\frac{h_0}{V} \tag{2.38}$$

Where:

- σ_c maximum stress before rupture;
- τ micro-structural rupture time;
- ν Poisson ratio;
- h_0 maximum approach between the two solids, with: m mass of the particle, V velocity of the particle;
- R radius of the particle.

To study the phenomenon of erosion on ductile material Professor I. Finnie [15] found an equation (2.39) to express the volume removed from a surface that is hit by particles.

$$V = \frac{c\,MU^2}{4p\left(1+\frac{mr^2}{I}\right)}\left[\cos^2\alpha - \left(\frac{\dot{x}_i}{U}\right)^2\right] \tag{2.39}$$

where:

- V volume removed from surface
- M mass of eroding particles;
- m mass of an individual particle;
- I moment of inertia of particle about its center of gravity;
- r average particle radius
- α angle of impact;
- U particle velocity;
- p horizontal component of flow pressure;
- c fraction of particles cutting in idealized manner;
- $\dot{x}_t$ horizontal velocity of tip of particle when cutting ceases.

In this study were used different assumptions:

- The displaced volume is the volume removed by the idealized particle;
- The particle is rigid and doesn't fracture;
- No initial rotation of the particles;
- Rotation of the particle is small during the cutting period;

- The configuration of the particle and of the deformed material is assumed to be geometrically similar during the cutting process;
- Since large strains will be reached even at the beginning of the cutting process, the plastic flow pressure between particle and metal will be constant;
- The area over which the metal contacts the particle is about twice that given by the depth of cut, represented with l in figure 2.9.

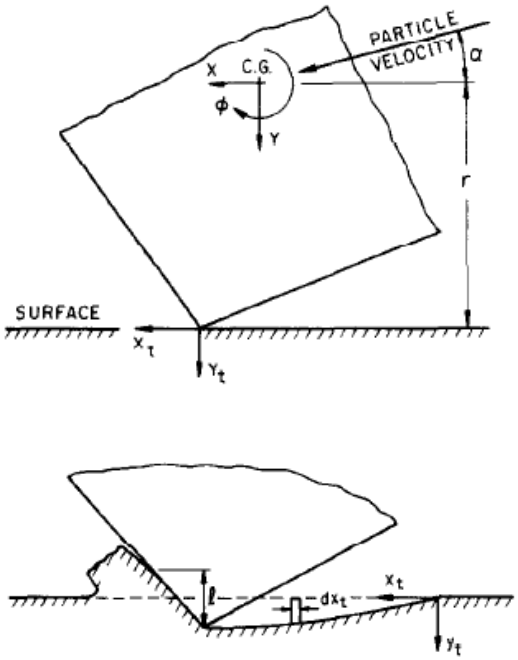

Figure 2.9: Idealized picture of an abrasive particle striking a surface and removing material [15]

2.6.2 Composite materials erosion mechanism

Polymer composite materials have lower erosion resistance compared to metallic materials [16], and the erosion wear of polymer composites is usually higher than that of the unreinforced polymer matrix [17]. In particular, polymer matrix composites with a thermosetting matrix consistently showed the highest erosion rate at high impact angles, indicating a brittle erosion behavior (generation and propagation of surface lateral cracks). In contrast, thermoplastic exhibited a peak erosion rate at intermediate impact angles, typically between 40° and 50°, suggesting a semi-ductile erosive wear (plastic deformation, ploughing, and ductile tearing)[16][18]. However, this failure classification is not absolute, as the erosion behavior of composites is highly influenced by experimental conditions[18].
The dimensionless erosion rate (E) is defined as the ratio between the mass loss of the eroded surface and the mass of the eroding particle responsible for the material removal. The Eq. 2.40 predict the erosion rate of a target surface [19]. It must be noted that this equation was obtained by studying the behaviour of the materials in table 2.1, i.e. thermoplastic polymers.

Sr. no.	Thermoplastic polymers	Density of composite (kg/m^3)	Vicker's hardness (Hv)
1	Polyetherimide (PEI)	1270	40.0
2	Polyetheretherketone (PEEK)	1300	28.0
3	Polyetherketone (PEK)	1300	34.4
4	Polyphenylene sulphide (PPS)	1400	26.5
5	Polyethersulfone (PES)	1370	24.2
6	Polysulfone (PSU)	1240	21.4

Table 2.1: Properties of Thermoplastic Polymers Composites

$$E_r = \frac{1}{6H_\nu} \cdot \eta \cdot \rho \cdot V^2 \cdot \left(\frac{2a \sin\alpha \cos\theta + 3h \cos\alpha}{a \sin\alpha \cos\theta + h \cos\alpha} \right) \tag{2.40}$$

where:

- α is the impact angle;
- H_V is the hardness;
- η is the erosion efficiency;
- V is the impact velocity;
- a and h are geometrical parameter of the erodent particle, defined in picture 2.10;
- ρ is the density of target material;
- E_r is the theoretical erosion wear rate.

In particular, erosion efficiency [20] is the ratio of fraction of volume that is removed to the crater volume formed by the erodent particle defined in Eq. (2.41).

$$Efficiency(\eta) = \frac{Volume\ removed}{Crater\ volume} \tag{2.41}$$

The assumptions for this model are:

- Erodent particle is rigid and does not deform during impact;
- The problem can be treated to be quasi-static, i.e. the dynamic affects such as wave propagation is neglected;
- Strain rate sensitivity is neglected;
- The only force assumed to be contact force exerted by the surface.

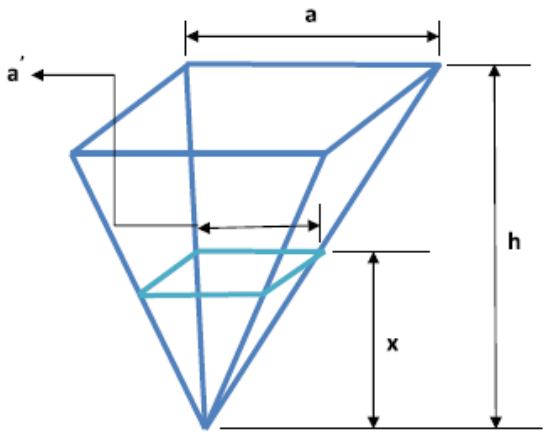

Figure 2.10: Erodent particle [19]

The study conducted by Anderson et al. [21] focuses on non-metallic materials, listed in table 2.2, which were part of a private research project at the Erosion/-Corrosion Research Center (E/CRC) and for confidentiality reasons, these materials were assigned alphabetical designations. They found a new equation to describe the erosion behaviour for non-metallic materials, reported in Eq.(2.42).

Material Name	**Material Type**	**Density (g/cm^3)**	**Shore D Value**
A	PEEK	1.30	88
R	PEEK	1.63	80
W	FRP	1.63	98
F	Elastomer	1.10	39

Table 2.2: Non-metallic material properties.

$$ER = k\, F_s\, F_{dp}\, V^n\, \mathrm{Norm}[F(\theta)] \tag{2.42}$$

with:

$$F_{dp} = \left(\frac{d_p}{300\,\mu m}\right)^{n_p} \tag{2.43}$$

$$\mathrm{Norm}[F(\theta)] = \frac{1}{f}\,(\sin\theta)^{n_1}\left(1+\left(\frac{SD}{75}\right)^{n_3}(1-\sin\theta)\right)^{n_2} \tag{2.44}$$

where:

- ER is the erosion ratio of eroded material;
- F_s and V are sand sharpness factor and particle impact velocity;
- F_{dp} and $F(\theta)$ are function to relate particle size and impact angle respectively;
- f is the maximum value of $F(\theta)$ to normalize the function

Empirical constants include the velocity exponent n with a standard value range of 2 to 3 based on material, and n_p is an empirical constant for particle size relation. Finally, n_1, n_2, and n_3 are empirical constants with SD being the material hardness in Shore D value[21].

2.7 Influence factors in erosion mechanism

Multiple factors play a role in the erosion mechanism [15] [22] [23]:

- Material hardness and impact angle;
- Particle velocity at impingement;
- Particle size;
- Shape of particle and strength;
- Surface properties;
- Particle concentration in fluid system;
- Particle rotation at impingement;
- Fiber orientation (for composite material);

Material hardness and impact angle

Material hardness is defined as the measure of a material's resistance to indentation and abrasion. This parameter influences the erosion rate. Hardness determines whether a material is ductile or brittle: ductile materials have low hardness, whereas brittle materials have high hardness. These two types of materials respond differently to the flow of erodent particles, figure 2.11.

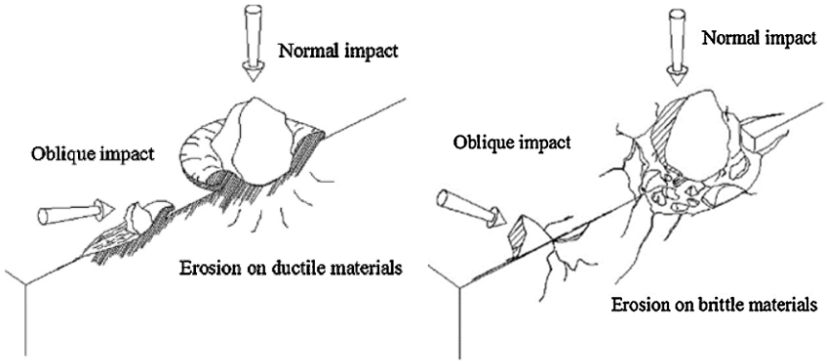

Figure 2.11: Erosion of ductile and brittle material[24]

The impact angle is defined as the angle beetween the eroded surface and the trajectory of the particle immediately before impact, and it is one of the most important parameters in erosive behavior. Considering the erosion rate as a function of the impingement angle, a significant difference was found between ductile and brittle materials. Ductile materials exhibit a maximum erosion rate at low impingement

angles 15-30^o. In contrast, brittle materials show the highest erosion rate at an impingement angle of 90^o, figure 2.12. Meanwhile, reinforced composites display a semi-ductile behavior, with maximum erosion occurring at angles within the range of 45-60^o. [25].

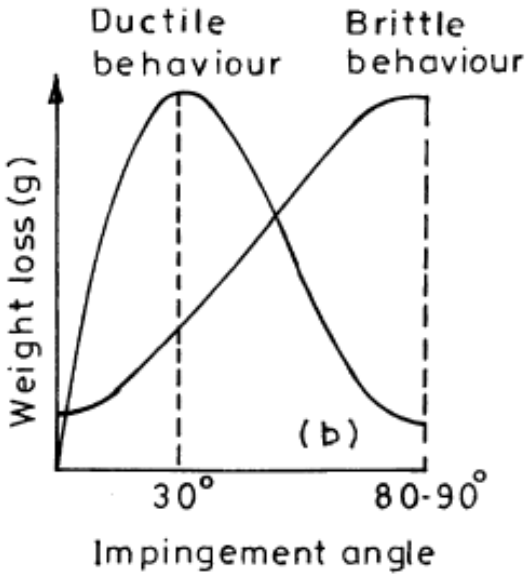

Figure 2.12: Schematic representation of brittle and ductile type of erosive wear

As mentioned above, ductile materials have a peak erosion rate of around 30^o. Miyazaki and Hamao [26], report the peak erosion for an unreinforced epoxy resin around 30^o.
Using carbon or glass fiber reinforced epoxy matrix composites [25]: RIGIDITE 5212 and 5217 epoxy prepreg system (BASF) reinforced with unidirectional celion G 30-500 carbon fibers and glass fibres with panels of 14 and 20 plies, was found that the erosion behavior of the above-mentioned composites is that the glass and carbon fibers used as reinforcement of the epoxy matrix are fragile materials, so erosion is due to damage mechanisms such as micro-cracking or plastic deformation. These mechanisms increase with the loss of kinetic energy, this is maximum for values of angles of impingement equal to 90^o, where the rate of erosion is maximum for fragile materials. It is concluded that the erosion rate peak shifts to higher values of impingement angle due to the brittle behavior of the fibers used[25].
In figure 2.13 can be seen that the weight loss is maximum at 60^o impingement angle for all fibre orientations for both materials.

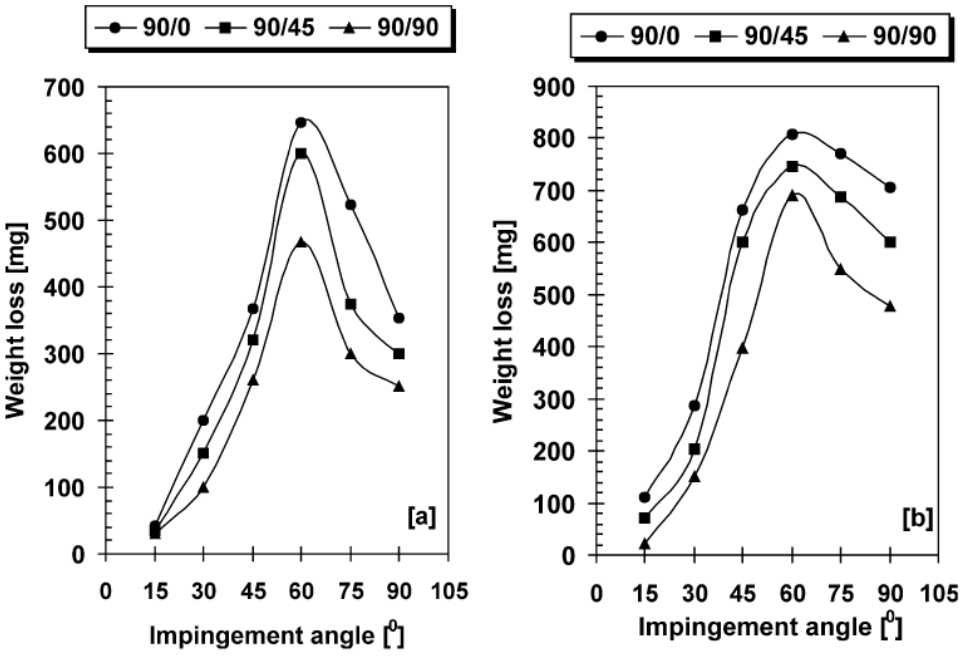

Figure 2.13: Influence of impingement angle, fibre orientations on the erosive wear of (a) CF/EP (b) GF/EP composites[25]

Particle velocity at impingement

An increase of particle velocity is an higher kinetic energy which results in higher erosion wear rate. This parameter strongly affects the erosion wear. In figure there is a comparison of erosion wear rate at impact velocity of 66 m/s and 25 m/s [19].

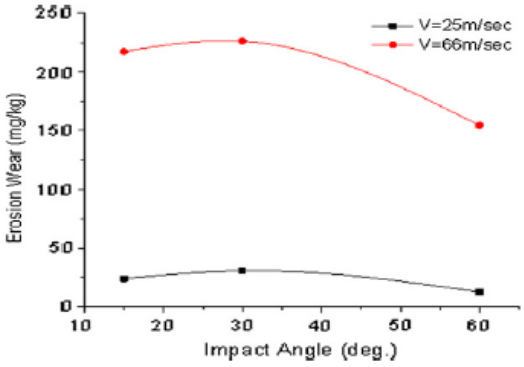

Figure 2.14: Comparison of erosion wear rate at impact velocity of 25 m/s and 66 m/s of Polyetherimide (PEI) polymer. [19]

Fiber orientation

Further research by Barkoula et al.[27] confirmed the theory that fiber orientation plays a significant role in determining the erosion behavior of composite materials during laboratory testing. They revealed that materials impacted parallel to the fiber orientation experienced greater matrix damage compared to those impacted perpendicularly.

However, adding complexity to the understanding of erosion mechanisms in composites, Pei et al.[28] reported opposite findings. In their study, materials with fibers oriented perpendicularly to the impact direction exhibited the most severe damage. SEM observations showed extensive matrix damage and removal, with the newly exposed fibers suffering greater damage than those aligned parallel to the impact direction[21].

Chapter 3

Material model

One of the objectives of this work is to develop a constitutive model for the damage focused on carbon fiber-reinforced thermoset composites. This goal is pursued with the use of the VUMAT subroutine, logical scheme in figure 3.1, developed at the ISAE Supaero by the department of mechanics, structures and materials. The purpose of this work is also to lay the foundation for validation of this VUMAT model for the study of the erosion phenomenon.
The main features of the model are discussed in the following chapters, for a complete understanding, reference should be made to the previous work, L.L. Pérez [3].

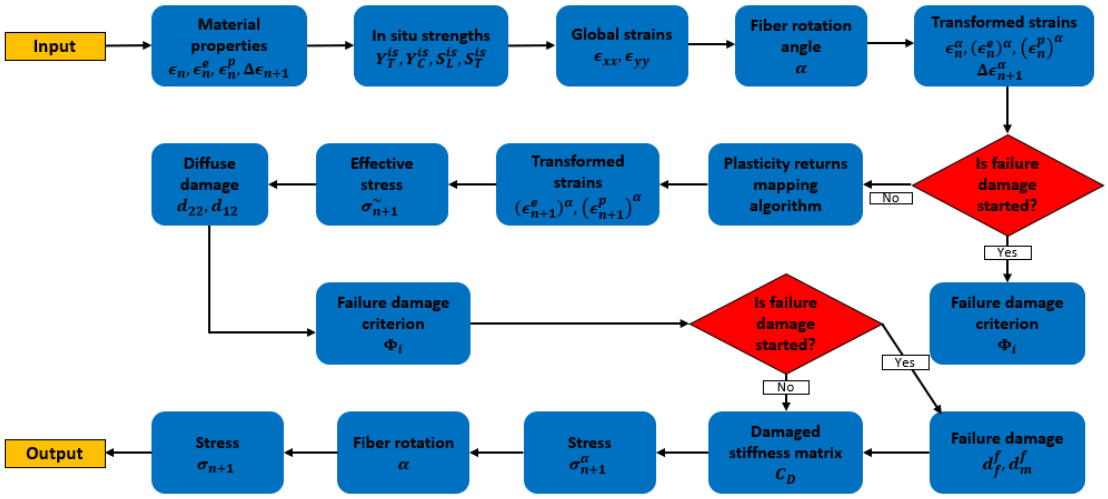

Figure 3.1: VUMAT logical scheme

3.1 In-situ Effect

When a multi-layered composite with different orientations is studied, the in-situ effect must be considered. Due to this response, when a ply is constrained between plies with different orientations, it exhibits higher transverse tensile and shear strengths than its equivalent in a unidirectional laminate. This effect also depends on the number of plies and their orientation [29]. To calculate the in-situ strengths three possible configurations are considered.

Thick ply

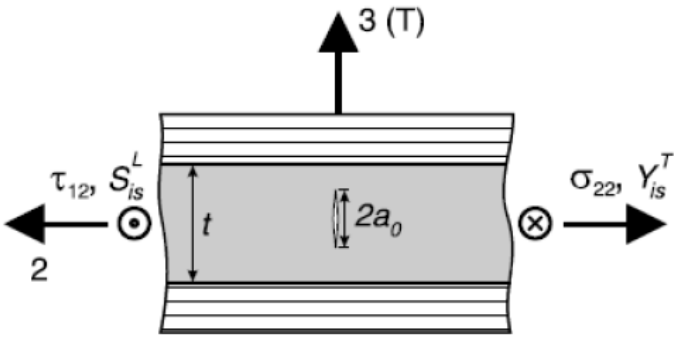

Figure 3.2: Thick ply [29]

In this configuration, figure 3.2, the transverse cracks in the matrix are shorter than ply thickness, in-situ transverse tensile strength is calculated with Eq. (3.1).

$$Y_T^{is} = \sqrt{\frac{2G_{I_c}(T)}{\pi a_0 \Lambda_{22}^0}} \tag{3.1}$$

Where $G_{Ic}(T)$ is the intralaminar critical energy release rate or fracture toughness for mode I crack growth in the direction of the thickness, and Λ_{22}^0 is calculated with the Eq.(3.2)

$$\Lambda_{22}^0 = 2\left(\frac{1}{E_2} - \frac{\nu_{21}^2}{E_1}\right) \tag{3.2}$$

The in-situ in-plane shear strength is calculated with Eq.(3.3).

$$S_L^{is} = \sqrt{\frac{(1+\beta\phi G_{12})^{\frac{1}{2}} - 1}{3\beta G_{12}}} \tag{3.3}$$

where β is a parameter that defines the non-linearity of the shear stress-shear strain relationship and ϕ is calculated with Eq.(3.4)

$$\phi = \frac{12S_L^2}{G_{12}} + 18\beta S_L^4 \tag{3.4}$$

Thin ply

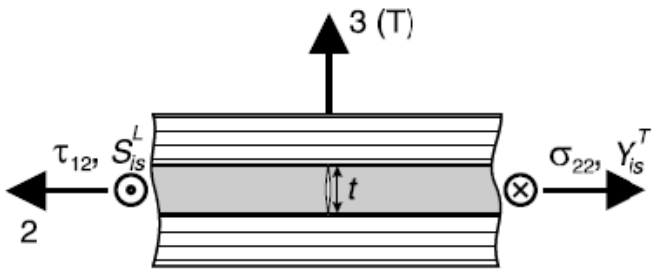

Figure 3.3: Thin ply [3]

In this configuration, the length of the transverse cracks in the matrix is equal to the thickness of the ply. With this configuration the in-situ tensile transverse strength is calculated with Eq.(3.5).

$$Y_T^{is} = \sqrt{\frac{8G_{Ic}(L)}{\pi t \Lambda_{22}^0}} \tag{3.5}$$

where t is the ply thickness and $G_{Ic}(L)$ is the intralaminar critical energy release rate or fracture toughness for mode I crack growth in the 1 direction.
The in-situ in-plane shear strength is calculated with the Eq.(3.3) but with the ϕ definition in Eq.(3.6).

$$\phi = \frac{48G_{IIc}(L)}{\pi t} \tag{3.6}$$

Thin outer ply

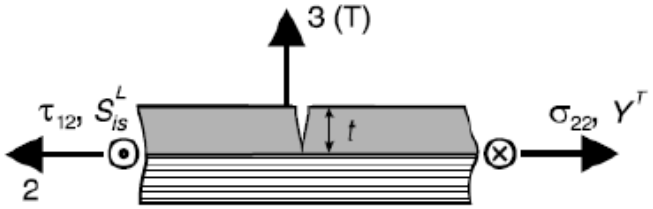

Figure 3.4: Thin outer ply[3]

This configuration is applied to the first or last ply of a laminate. The in-situ tensile transverse strength is calculated with Eq. where ϕ is (3.7).

$$Y_T^{ts} = \sqrt{\frac{4G_{Ic}(L)}{\pi t \Lambda_{22}^0}} \tag{3.7}$$

Even in this case the in-situ in-plane shear strength is calculated with Eq.(3.3), where ϕ is calculated with Eq.(3.8)

$$\phi = \frac{24G_{IIc}(L)}{\pi t} \tag{3.8}$$

For the calculation of the in-situ compressive transverse strength (Y_C^{is} and the in-situ through the thickness strength (S_T^{is}) are used the Eq.(3.9) and Eq.(3.10) respectively, that were proposed by Catalanotti et al.[30].

$$Y_C^{is} = -\frac{S_L^{is}(2\cos^2(\alpha_0) - 1)}{\eta_L \cos^2(\alpha_0)} \tag{3.9}$$

$$S_T^{is} = \frac{S_L^{is}(2\sin^2(\alpha_0) - 1)}{2\eta_L \sqrt{1 - \sin^2(\alpha_0)} \sin(\alpha_0)} \tag{3.10}$$

where $\alpha_0 = 53 \pm 2°$ is the fracture angle under pure transverse compression [31] and η_L is the longitudinal friction coefficient, that can be calculated using Eq.(3.11) and Eq.(3.12)[3].

$$\eta_T = -\frac{1}{\tan(2\alpha_0)} \tag{3.11}$$

$$\frac{\eta_L}{S_L} = \frac{\eta_T}{S_T} \tag{3.12}$$

3.2 Fiber rotation

When a load is applied to a composite material the fibers tend to rotate in the direction of application of the load, this can lead to a rotation of the fibers by about 10° [32]. To consider this phenomenon in VUMAT, the equation of J.Fuller & M.Wisnom[3] is using. The rotation of the fibers respect to original fiber position is calculated with equation (3.13).

$$\theta = \arctan\left(\frac{\tan(\theta_0) + \varepsilon_{yy}}{1 + \varepsilon_{xx}}\right) \tag{3.13}$$

Where θ_0 is the fiber orientation in the undeformed material. Since Abaqus computes stress and strain increments in the "material" coordinate system, which corresponds to the lamina coordinate system of the undamaged material, fiber rotation must be determined at the start of each iteration, and strains should be evaluated in the "rotated" coordinate system.

3.3 Diffuse damage

In the VUMAT diffuse damage model [3], two damage variables are defined,d_{22} and d_{12}, which are respectively associated with transverse matrix micro-cracking and fiber-matrix debonding. In VUMAT subroutine there are three possible diffuse damage model: Ladeveze model, Wang model and expanded model.
The Wang model works with just two diffuse damage variables and to take into account crack closure. The expanded model uses the same damage variables and damage evolution laws as the Ladeveze model, but expands the definition of the Helmholtz free energy density to include terms related to a three dimensional case. The model proposed by P. Ladeveze and E. Le Dantec in 1992 [33] defines the Helmholtz free energy density as shown in Eq.(3.14).

$$\Psi = \frac{1}{2\rho}\left[\frac{\sigma_{11}^2}{E_1} + \frac{\langle\sigma_{22}\rangle_+^2}{E_2(1-d')} + \frac{\langle\sigma_{22}\rangle_-^2}{E_2} - 2\frac{\nu_{12}\sigma_{11}\sigma_{22}}{E_1} + \frac{\sigma_{12}^2}{G_{12}(1-d)}\right] \tag{3.14}$$

Where $\langle x\rangle$ are the Macaulay brackets:

$$\langle x\rangle_+ = \begin{cases} 0, & x < 0 \\ x, & x \geq 0 \end{cases} \tag{3.15}$$

$$\langle x\rangle_- = \begin{cases} x, & x \leq 0 \\ 0, & x > 0 \end{cases} \tag{3.16}$$

The Macaulay brackets are employed to account for crack closure under compression. d and d' are the scalar damage variables, defined in Eq.(3.17) and (3.18) ; this model considers two distinct degradation mechanisms. The first mechanism, associated with the damage variable d, corresponds to fiber-matrix debonding. The second mechanism, linked to the damage variable d', represents matrix microcracking.

$$d = \begin{cases} \frac{\langle Y - Y_0 \rangle_+}{Y_c}, & d < 1 \text{ and } Y' < Y'_s \\ 1, & \text{otherwise} \end{cases} \tag{3.17}$$

$$d' = \begin{cases} \frac{\langle Y - Y'_0 \rangle_+}{Y'_c}, & d' < 1 \text{ and } Y' < Y'_s \\ 1, & \text{otherwise} \end{cases} \tag{3.18}$$

Where:

$$Y(t) = \sup_{\tau \leq t} \left(\sqrt{Y_d(\tau) + bY_{d'}(\tau)} \right) \tag{3.19}$$

$$Y'(t) = \sup_{\tau \leq t} \left(\sqrt{Y_{d'}(\tau)} \right) \tag{3.20}$$

The parameters Y_c, Y'_c, Y_0, Y'_c and b depend on material characteristics, while Y'_s indicates the brittle damage threshold of the fiber-matrix interface under transverse tension[3]. In particular, Y_d and $Y_{d'}$ are the associated thermodynamic forces, that are analogous to energy-release rates, and regulate damage evolution similarly to how energy release rates control crack propagation[33]. They are calculated with Eq. (3.21) and (3.22).

$$Y_d = -\rho \frac{\partial \Psi}{\partial d} = \frac{\sigma_{12}^2}{2G_{12}(1-d)^2} \tag{3.21}$$

$$Y_{d'} = -\rho \frac{\partial \Psi}{\partial d'} = \frac{\langle \sigma_{22} \rangle_+^2}{2E_{12}(1-d')^2} \tag{3.22}$$

In the Wang model is used the Helmoholtz free energy density as defined in Eq.(3.23) [3].

$$\begin{aligned} \Psi = \frac{1}{2\rho} \Bigg[& \frac{\sigma_{11}^2}{E_1} + \frac{\sigma_{22}^2}{E_2(1-d_{22})} + \frac{\sigma_{33}^2}{E_3} + \\ & - 2\frac{\nu_{12}\sigma_{11}\sigma_{22}}{E_1} - 2\frac{\nu_{13}\sigma_{11}\sigma_{33}}{E_1} - 2\frac{\nu_{23}\sigma_{22}\sigma_{33}}{E_2} + \\ & + \frac{\sigma_{12}^2}{G_{12}(1-d_{12})} + \frac{\sigma_{13}^2}{G_{13}} + \frac{\sigma_{23}^2}{G_{23}} \Bigg] \end{aligned} \tag{3.23}$$

To control how the values of diffuse damage variables change are used Eq.(3.24) and Eq.(3.25)[3].

$$d_{22} = \begin{cases} a_d Y_{d_{22}}, & Y_{d_{22}}^0 \leq Y_{d_{22}} < Y_{d_{22}}^c \\ 0, & \text{otherwise} \end{cases} \tag{3.24}$$

$$d_{12} = \begin{cases} b_d Y_{d_{12}} + c_d, & Y_{d_{12}}^0 \leq Y_{d_{12}} < Y_{d_{12}}^{trans} \\ d_d Y_{d_{12}}^{e_d} + f_d, & Y_{d_{12}}^{trans} \leq Y_{d_{12}} < Y_{d_{12}}^c \\ 0, & \text{otherwise} \end{cases} \tag{3.25}$$

Where a_d, b_d, c_d , d_d, e_d, f_d, Y^o_{d22}, Y^o_{d12} and Y^{trans}_{d12} are experimentl data; Y_{d22} and Y_{d12} are calculated like in the Ladeveze model, with Eq.(3.26) and Eq.(3.27).

$$Y_{d_{22}}(t) = \sup_{\tau \leq t} \left(\sqrt{Y_{d_{22}}(\tau)} \right) \tag{3.26}$$

$$\overline{Y}_{d_{12}}(t) = \sup_{\tau \leq t} \left(\sqrt{Y_{d_{12}}(\tau)} + b\overline{Y}_{d_{22}}(\tau) \right) \tag{3.27}$$

Where b is a material characteristic[33].

In the custom model the definition of Helmholtz free energy density is given by Eq.(3.28)

$$\begin{aligned} \Psi = \frac{1}{2\rho} \Bigg[& \frac{\sigma_{11}^2}{E_1} + \frac{\langle \sigma_{22} \rangle_+^2}{E_2(1-d_{22})} + \frac{\langle \sigma_{22} \rangle_-^2}{E_2} + \frac{\langle \sigma_{33} \rangle_+^2}{E_3(1-d_{22})} \\ & + \frac{\langle \sigma_{33} \rangle_-^2}{E_3} - 2\frac{\nu_{12}\sigma_{11}\sigma_{22}}{E_1} - 2\frac{\nu_{13}\sigma_{11}\sigma_{33}}{E_1} \\ & - 2\frac{\nu_{23}\sigma_{22}\sigma_{33}}{E_2} + \frac{\sigma_{12}^2}{G_{12}(1-d_{12})} + \frac{\sigma_{13}^2}{G_{13}(1-d_{12})} \\ & + \frac{\sigma_{23}^2}{G_{23}(1-d_{12})} \Bigg] \end{aligned} \tag{3.28}$$

3.4 Plasticity effect

To simulate the plastic behavior of the material, it is necessary to define a plastic potential function, a hardening law and an algorithm that calculates plastic deformation. In plasticity theory, the material only experiences elastic deformation until the yield surface is reached. This is expressed with the yield function:

$$F_p(\tilde{\sigma}, p) = f_p(\tilde{\sigma}) - \sigma_y(p) \leq 0 \tag{3.29}$$

where $f_p(\tilde{\sigma})$ is the plastic potential function and $\sigma_y(p)$ is the yield stress, whose definition depends on the hardening law[3].

For the VUMAT subroutine, the Hill-type plastic potential function [34], independent of longitudinal effective stresses, is chosen.

$$f_p(\tilde{\sigma}) = \sqrt{\tilde{\sigma}_{12}^2 + \tilde{\sigma}_{13}^2 + \tilde{\sigma}_{23}^2 + a^2(\tilde{\sigma}_{22}^2 + \tilde{\sigma}_{33}^2)} \tag{3.30}$$

where the parameter a describes the relationship between plastic deformation induced by transverse loads and that caused by shear loads, determined experimentally and defined by the Equation 3.31.

$$a^2 = \frac{\dot{\varepsilon}^p_{22}(1-d_{22})^2\sigma_{12}}{2\dot{\varepsilon}^p_{12}(1-d_{12})^2\sigma_{22}} \tag{3.31}$$

The use of σ_{ij} effective stress components in the plastic potential arises from the concept that the internal stress generated under loading is carried by the undamaged

portion of the material.
The hardening law used was derived from experimental data obtained from tensile tests on $AS4/PEEK$ coupons with a stacking sequence of $[\pm 45°]_{2S}$, reported in Equation 3.32 [3].

$$\sigma_y(p) = K(p + \beta_p)^{\alpha_p} \tag{3.32}$$

where K, α_p and β_p are parameters obtained from experimental data.
p, defined in Equation 3.33 , also accounts for the effect of damage in the measured plastic strain, ensuring the effective accumulated plastic strain is obtained.

$$p = s(1 - d_{12})\varepsilon_{12}^p \tag{3.33}$$

In this case the most appropriate algorithm is a cutting plane algorithm (CPA) that convergence within a reasonable and consistently stable number of iterations, Figure 3.5.

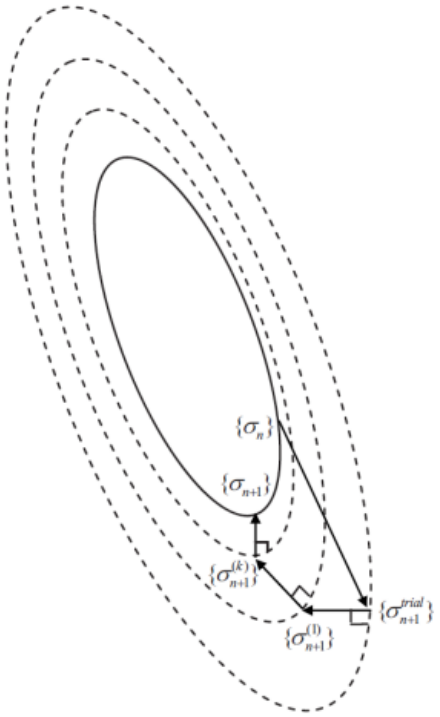

Figure 3.5: Stress returns CPA

The way plastic strain is calculated at any time step is here presented:

Step 1: Trial stress

If the strain increment during the time step were purely elastic the effective stress, also called effective proof stress, would be obtained with Equation 3.34[**Luis la**].

$$\tilde{\sigma}_{trial} = C : (\varepsilon_{n+1} - \varepsilon_n^p) \tag{3.34}$$

dove

- ε_n^p is the plastic strain tensor at the beginning of the current time step, which is known since it corresponds to that at the end of the previous time step;
- ε_{n+1} is the total strain tensor at the end of the current time step, known because Abaqus calculates the total strain increments at each time step;
- C is the stiffness tensor.

Step 2: Initial check of the Yield condition

Using the trial effective stress and the accumulated plastic strain value at the beginning of the time step, the yield function is evaluated Equation 3.35.

$$F_p(\tilde{\sigma}_{trial}, p_n) = f_p(\tilde{\sigma}_{trial}) - \sigma_y(p_n) \tag{3.35}$$

If $F_p(\tilde{\sigma}_{trial}, p_n) \leq 0$ only elastic deformation occurred since the yield surface was not exceeded. In this case elastic strain in calculated as $\varepsilon_{n+1}^e = \varepsilon_{n+1} - \varepsilon_n^p$, plastic strain as ε_{n+1} and acculated plastic strain p_{n+1} are the same as in the previous step.
If $F_p(\tilde{\sigma}_{trial}, p_n) > 0$, plastic deformation has occurred, as the yield surface has been exceeded. In this case, the condition $F_p(\tilde{\sigma}_{n+1}, p_{n+1}) = 0$ is obtained, derived from the Kuhn-Tucker conditions. Therefore, the value of the plastic strain rate $\dot{\lambda}$ must be determined such that $F_p = 0$. However, this process would be too time-consuming, so the condition $|F_p| \leq TOL$ is accepted instead.

Step 3: Initialization

Before applying the iterative CPA algorithm, some initial values must be defined.

$$F_p^0 = F_p(\tilde{\sigma}_{trial}, p_n), \quad \varepsilon_{n+1}^{p0} = \varepsilon_n^p, \quad p_{n+1}^0 = p_n \tag{3.36}$$

The initial value for the gradient of the yield function with respect to stresses of plastic flow is defined in Equation 3.37.

$$a^0 = \left.\frac{\partial F_p}{\partial \tilde{\sigma}}\right|_{\tilde{\sigma}_{trial}, p_n} = \frac{1}{f_p(\tilde{\sigma}_{trial})} \begin{Bmatrix} 0 \\ c^2\tilde{\sigma}_{22trial} \\ c^2\tilde{\sigma}_{33trial} \\ \tilde{\sigma}_{12trial} \\ \tilde{\sigma}_{13trial} \\ \tilde{\sigma}_{23trial} \end{Bmatrix} \tag{3.37}$$

Step 4: Plastic strain rate

This marks the initial step of the CPA algorithm, where the plastic strain rate is computed with Equation 3.38.

$$\dot{\lambda}^{i+1} = \frac{F_p^i}{\mathbf{a}^{iT} : C : \mathbf{a}^i + H^i} \tag{3.38}$$

where H^i is calculated with Equation 3.39.

$$H^i = \left.\frac{\partial \sigma_y}{\partial p}\right|_{p_{n+1}^i} = K\alpha_p \left(p_{n+1}^i + \beta_p\right)^{(\alpha_p - 1)} \tag{3.39}$$

Step 5: Plastic strain

Plastic strain is calculated with Equation 3.40.

$$\varepsilon_{n+1}^{pi+1} = \varepsilon_{n+1}^{pi} + \delta\varepsilon_{n+1}^{pi+1} = \varepsilon_{n+1}^{pi} + \dot{\lambda}^{i+1}\mathbf{a}^{i} \tag{3.40}$$

Step 6: Effective strain

Then effective stress increment if found with Equation 3.41.

$$\tilde{\sigma}^{i+1} = \tilde{\sigma}^{i} + \delta\tilde{\sigma}^{i+1} = \tilde{\sigma}^{i} - \dot{\lambda}^{i+1}C : \mathbf{a}^{i} \tag{3.41}$$

Step 7: Accumulated plastic strain

The accumulated plastic strain is updated with Equation 3.42.

$$p_{n+1}^{i+1} = p_{n+1}^{i} + \dot{\lambda}^{i+1} \tag{3.42}$$

Step 8: Plastic flow

Using the effective stress computed in Step 6, the plastic flow is reported in Equation 3.43

$$a^{i+1} = \left.\frac{\partial F_p}{\partial\tilde{\sigma}}\right|_{\tilde{\sigma}^{i+1},p_{n+1}^{i+1}} = \frac{1}{f_p(\tilde{\sigma}^{i+1})}\begin{Bmatrix} 0 \\ c^2\tilde{\sigma}_{22}^{i+1} \\ c^2\tilde{\sigma}_{33}^{i+1} \\ \tilde{\sigma}_{12}^{i+1} \\ \tilde{\sigma}_{13}^{i+1} \\ \tilde{\sigma}_{23}^{i+1} \end{Bmatrix} \tag{3.43}$$

Step 9: Yield condition

The final step of the CPA algorithm is to verify whether the yield condition satisfies the tolerance requirement using the values computed in the last iteration. The yield function is calculated with Equation 3.44.

$$F_p^{i+1} = F_p(\tilde{\sigma}^{i+1}, p_{n+1}^{i+1}) = f_p(\tilde{\sigma}^{i+1}) - \sigma_y(p_{n+1}^{i+1}) \tag{3.44}$$

If $|F_p^{i+1}| \leq TOL$, then a solution has been found. The last calculated values in steps 4 to 9 can be saved as correct values.
If $|F_p^{i+1}| > TOL$, then a solution has not been found. In this case, $i = i + 1$ and start again the process from Step 4.

3.5 Failure criterion

The failiure criterion that is implemented in VUMAT is the interactive Catalotti criterion with the addition of a further failure index[30]. This criterion distinguishes different failure modes related to fiber or matrix failure under tension or compression and incorporates in-situ effects in its formulation.

For the computation for the tensile matrix failure this model used the failure index in Eq.(3.45) [3].

$$.\Phi_{mt} = \begin{cases} 0, & \sigma_n < 0 \\ \left(\frac{\sigma_n}{S_T^{is}}\right)^2 + \left(\frac{\tau_L}{S_L^{is}}\right)^2 + \left(\frac{\tau_T}{S_T^{is}}\right)^2 + \lambda\left(\frac{\sigma_n}{S_T^{is}}\right)\left(\frac{\tau_L}{S_L^{is}}\right)^2 + \kappa\left(\frac{\sigma_n}{S_T^{is}}\right), & \sigma_n \geq 0 \end{cases} \tag{3.45}$$

Where the parameters κ and λ can be calculated with the Eq.(3.46).

$$\kappa = \frac{(S_T^{is})^2 - (Y_T^{is})^2}{S_T^{is} Y_T^{is}} \quad \lambda = 2\eta_L \frac{S_T^{is}}{S_L^{is}} - \kappa \tag{3.46}$$

There are the loading cases for which the failure index is negative; in particular, when κ is negative that depending on the in-situ strengths of the material.
Stress components on the fracture plane are calculated with Eq.(3.47)

$$\begin{aligned} \sigma_n &= \frac{\tilde{\sigma}_{22} + \tilde{\sigma}_{33}}{2} + \frac{\tilde{\sigma}_{22} - \tilde{\sigma}_{33}}{2}\cos(2\alpha) + \tilde{\sigma}_{23}\sin(2\alpha) \\ \tau_L &= -\frac{\tilde{\sigma}_{22} - \tilde{\sigma}_{33}}{2}\sin(2\alpha) + \tilde{\sigma}_{23}\cos(2\alpha) \\ \tau_T &= \tilde{\sigma}_{12}\cos(\alpha) + \tilde{\sigma}_{13}\sin(\alpha) \end{aligned} \tag{3.47}$$

To determine the fracture plane angle α, the failure index for tensile matrix failure is evaluated for all possible fracture plane angles between 0^o and 90^o degrees. The correct fracture plane angle is identified as the one corresponding to the maximum value of either the tensile or compressive matrix failure index, whichever is greater.

To evaluate the compressive matrix failure index it is used a modified version of the failure criterion proposed by A.Puck & H.Schürmann [31], reported in Eq.(3.48).

$$\Phi_{mc} = \begin{cases} \left(\frac{\tau_T}{S_T^{is} - \eta_T \sigma_n}\right)^2 + \left(\frac{\tau_L}{S_L^{is} - \eta_L \sigma_n}\right)^2, & \sigma_n < 0 \\ 0, & \sigma_n \geq 0 \end{cases} \tag{3.48}$$

The stressed on the fracture plane are, even in compression, evaluate with Eq.(3.47). To evaluate tensile fiber failure and compressive fiber failure a non-interacting maximum strain criterions are used[30], respectively Eq.(3.49) and Eq.(3.50).

$$\Phi_{ft} = \begin{cases} 0, & \varepsilon_{11} < 0 \\ \frac{\varepsilon_{11}}{\varepsilon_{11}^T}, & \varepsilon_{11} \geq 0 \end{cases} \tag{3.49}$$

$$\Phi_{fC} = \begin{cases} \frac{\varepsilon_{11}}{\varepsilon_{11}^C}, & \varepsilon_{11} < 0 \\ 0, & \varepsilon_{11} \geq 0 \end{cases} \tag{3.50}$$

Where ε_{11}^{fT} is the tensile failure strain in the direction of the fiber and ε_{11}^{fC} is the compressive failure strain in fiber direction.

3.5.1 Fiber kinking

The formation of kink bands results from the rotation of initially misaligned fibers, causing shear deformation in the matrix. Two failure indexes, associated to this phenomenon, were proposed by Catalanotti et al. [30], Eq.(3.51) and Eq.(3.52).

$$\Phi_{fkT} = \begin{cases} 0, & \sigma_n^{(m)} < 0 \\ \left(\frac{\sigma_n^{(m)}}{S_T^{is}}\right)^2 + \left(\frac{\tau_L^{(m)}}{S_L^{is}}\right)^2 + \left(\frac{\tau_T^{(m)}}{S_T^{is}}\right)^2 + \lambda\left(\frac{\sigma_n^{(m)}}{S_T^{is}}\right)\left(\frac{\tau_L^{(m)}}{S_L^{is}}\right)^2 + \kappa\left(\frac{\sigma_n^{(m)}}{S_T^{is}}\right), & \sigma_n^{(m)} \geq 0 \end{cases} \tag{3.51}$$

$$\Phi_{fkC} = \begin{cases} \left(\frac{\tau_T^{(m)}}{S_T^{is} - \eta_T \sigma_n^{(m)}}\right)^2 + \left(\frac{\tau_L^{(m)}}{S_L^{is} - \eta_L \sigma_n^{(m)}}\right)^2, & \sigma_n^{(m)} < 0 \\ 0, & \sigma_n^{(m)} \geq 0 \end{cases} \tag{3.52}$$

Where the chosen one depends on the value of the resulting stresses on fracture plane, if is under tension or compression.
The normal and shear stresses on the fracture plane can be evaluated with Eq.(3.53) and Eq.(3.54)(3.55), respectively.

$$\sigma_n^{(m)} = \tilde{\sigma}_{22}^{\alpha} = \frac{\tilde{\sigma}_{22}^{\theta} + \tilde{\sigma}_{33}^{\theta}}{2} + \frac{\tilde{\sigma}_{22}^{\alpha} - \tilde{\sigma}_{33}^{\theta}}{2}\cos(2\alpha) + \tilde{\sigma}_{23}^{\alpha}\sin(2\alpha) \tag{3.53}$$

$$\tau_T^{(m)} = \tilde{\sigma}_{23}^{(\alpha)} = -\frac{\tilde{\sigma}_{22}^{(\varphi)} - \tilde{\sigma}_{33}^{(\theta)}}{2}\sin(2\alpha) + \tilde{\sigma}_{23}^{(\varphi)}\cos(2\alpha) \tag{3.54}$$

$$\tau_L^{(m)} = \tilde{\sigma}_{12}^{(\alpha)} = \tilde{\sigma}_{12}^{(\varphi)}\cos(\alpha) + \tilde{\sigma}_{13}^{(\varphi)}\sin(\alpha) \tag{3.55}$$

where $\tilde{\sigma}_{22}^{(\alpha)}$, $\tilde{\sigma}_{23}^{(\alpha)}$ and $\tilde{\sigma}_{12}^{(\alpha)}$ are effective stress components on the third of the three coordinate systems associated with fiber kinking, $\tilde{\sigma}_{22}^{(\varphi)}$, $\tilde{\sigma}_{12}^{(\varphi)}$, and $\tilde{\sigma}_{13}^{(\varphi)}$ are effective stress components on the second of the three coordinate systems associated with fiber kinking, and $\tilde{\sigma}_{33}^{(\theta)}$ is an effective stress component on the first of the three coordinate systems associated with fiber kinking[3].
To obtain the effective stress tensors in these coordinate systems, the following coordinate transformations must be performed.

$$\begin{aligned} \tilde{\sigma}^{(\theta)} &= R_{()\to(\theta)} \to \tilde{\sigma}\, R_{()\to(\theta)}^T \\ \tilde{\sigma}^{(\varphi)} &= R_{(\theta)\to(\varphi)} \to \tilde{\sigma}\, R_{(\theta)\to(\varphi)}^T \\ \tilde{\sigma}^{(\alpha)} &= R_{(\varphi)\to(\alpha)} \to \tilde{\sigma}\, R_{(\varphi)\to(\alpha)}^T \end{aligned} \tag{3.56}$$

where:

$$R_{()\to(\theta)} = \begin{bmatrix} 1 & 0 & 0 \\ 0 & \cos(\theta) & \sin(\theta) \\ 0 & -\sin(\theta) & \cos(\theta) \end{bmatrix} \tag{3.57}$$

$$R_{(\theta)\to(\varphi)} = \begin{bmatrix} \cos(\varphi) & \sin(\varphi) & 0 \\ -\sin(\varphi) & \cos(\varphi) & 0 \\ 0 & 0 & 1 \end{bmatrix} \tag{3.58}$$

$$R_{(\varphi)\to(\alpha)} = \begin{bmatrix} 1 & 0 & 0 \\ 0 & \cos(\alpha) & \sin(\alpha) \\ 0 & -\sin(\alpha) & \cos(\alpha) \end{bmatrix} \tag{3.59}$$

Tha angles θ ang φ are calculated with Equation 3.60 and 3.61.

$$\theta = \frac{1}{2} \arctan\left(\frac{2\tilde{\sigma}_{23}}{\tilde{\sigma}_{22} - \tilde{\sigma}_{33}}\right) \tag{3.60}$$

$$\varphi = \begin{cases} -\gamma_m & \tilde{\sigma}_{12} < 0 \\ \gamma_m & \tilde{\sigma}_{12} \geq 0 \end{cases} \tag{3.61}$$

The parameter γ_m is computed numerically using the Newton-Raphson method. Convergence is achieved by comparing the relative error of γ_m between successive iterations with a predefined tolerance threshold.
The angle α is determined similarly to the fracture angle in tensile and compressive failure cases. Both Φ_{fkT} and Φ_{fkC} are evaluated for all possible values of α within the range of 0° to 90°. The angle corresponding to the maximum index is selected as the correct α value.

3.6 Failure damage

After the material has failed, its post-failure behavior is governed by the failure damage model. In the VUMAT as failure damage model is based on the Linde model [35]. Proposed by P. Linde et al. in 2004 to simulate the behavior of fiber-metal laminates, this model introduces an exponential law governed by the fracture energies of both the fibers and the matrix. The failure damage model employs two distinct damage variables: one representing fiber failure and the other representing matrix failure. The failure damage evolution are Eq.(3.62) and Eq.(3.63)

$$d_f^f = 1 - \frac{1}{\Phi_f} \exp\left(\frac{(1-\Phi_f) C_{11} L_c (\varepsilon_{11}^f)^2}{G_{f_c}}\right) \tag{3.62}$$

$$d_m^f = 1 - \frac{1}{\Phi_m} \exp\left(\frac{(1-\Phi_m) C_{22} L_c (\varepsilon_{22}^f)^2}{G_{m_c}}\right) \tag{3.63}$$

Where d_f^f is the failure damage variable for fiber failure, d_m^f is the failure damage variable for matrix failure, L_c is the characteristic element length, G_{fc} is the fracture energy of the fibers, G_{mc} is the fracture energy of the matrix and ε_{ii}^f are the failure strains in the i direction.
A modified model is used in the VUMAT to be compatible with the Catalanotti failure criterion.

Matrix Failure Damage

The Catalanotti failure criterion contains four failure indices related to matrix failure. The impact of the different failure modes on the material's behavior must be represented by a single matrix failure damage variable. To achieve this, the matrix failure damage variable is calculated separately for each failure mode and then combined into a single value that characterizes the overall matrix damage.
In particular, the matrix failure damage variable is computed separately for tensile

and compressive loading conditions to accurately represent the material behavior under different stress states, reported in Eq.(3.64) and Eq.(3.65) respectively.

$$d_{mt}^{f} = 1 - \frac{1}{\Phi_{mt}} \exp\left(\frac{(1-\Phi_{mt}) C_{22} L_c \left\langle \varepsilon_{eq}^{fT(\alpha)} \right\rangle^2}{G_{mc}^{T}} \right) \tag{3.64}$$

$$d_{mc}^{f} = 1 - \frac{1}{\Phi_{mc}} \exp\left(\frac{(1-\Phi_{mc}) C_{22} L_c \left\langle \varepsilon_{eq}^{fC(\alpha)} \right\rangle^2}{G_{mc}^{C}} \right) \tag{3.65}$$

where G_{mc}^{T} and G_{mc}^{C} are the intralaminar fracture toughnesses of the matrix under tension and compression respectively.
If longitudinal compression occurs ($\tilde{\sigma}_{11} < 0$), fiber kinking must also be considered, Eq.(3.66) and Eq.(3.67). Where d_{fkT}^{f} and d_{fkC}^{f} are the matrix failure damage variables associated with fiber kinking damage in tension and compression, respectively.

$$d_{fkT}^{f} = 1 - \frac{1}{\Phi_{fkT}} \exp\left(\frac{(1-\Phi_{fkT}) C_{22} L_c \left\langle \varepsilon_{eq}^{fkT(\alpha)} \right\rangle^2}{G_{mc}^{T}} \right) \tag{3.66}$$

$$d_{fkC}^{f} = 1 - \frac{1}{\Phi_{fkC}} \exp\left(\frac{(1-\Phi_{fkC}) C_{22} L_c \left\langle \varepsilon_{eq}^{fkC(\alpha)} \right\rangle^2}{G_{mc}^{C}} \right) \tag{3.67}$$

To perform these calculations, the equivalent failure strain must be computed on the fracture plane. In the subroutine, this equivalent failure strain is stored for each failure mode when the corresponding failure index reaches a value of one. This equivalent failure strain is calculated with Eq.(3.68).

$$\varepsilon_{eq}^{f(\alpha)} = \sqrt{\left\langle \varepsilon_{n}^{f} \right\rangle^2 + \left\langle \gamma_{T}^{f} \right\rangle^2 + \left\langle \gamma_{L}^{f} \right\rangle^2} = \sqrt{\left\langle \varepsilon_{22}^{f(\alpha)} \right\rangle^2 + \left\langle 2\varepsilon_{23}^{f(\alpha)} \right\rangle^2 + \left\langle 2\varepsilon_{12}^{f(\alpha)} \right\rangle^2} \tag{3.68}$$

The value of the matrix failure damage is obtained with Eq.(3.69)

$$d_{m}^{f} = \begin{cases} \max\left(d_{mt}^{f}, d_{fkt}^{f}\right) + d_{mc}^{f}, & \varepsilon_{22}^{e} \geq 0 \text{ and } \tilde{\sigma}_{11} < 0 \text{ and } \max\left(d_{mt}^{f}, d_{fkt}^{f}\right) + d_{mc}^{f} < 1 \\ \max\left(d_{mc}^{f}, d_{fkc}^{f}\right), & \varepsilon_{22}^{e} < 0 \text{ and } \tilde{\sigma}_{11} < 0 \text{ and } \max\left(d_{mc}^{f}, d_{fkc}^{f}\right) < 1 \\ d_{mt}^{f} + d_{mc}^{f}, & \varepsilon_{22}^{e} \geq 0 \text{ and } \tilde{\sigma}_{11} \geq 0 \text{ and } d_{mt}^{f} + d_{mc}^{f} < 1 \\ d_{mc}^{f}, & \varepsilon_{22}^{e} < 0 \text{ and } \tilde{\sigma}_{11} \geq 0 \text{ and } d_{mc}^{f} < 1 \\ 1, & \text{otherwise} \end{cases} \tag{3.69}$$

To guarantee the irreversibility of the damage is used Eq.(3.70).

$$d_{m}^{f} = \sup_{\tau \leq t} \left(d_{m}^{f'} \right) \tag{3.70}$$

Fiber Failure Damage

Catalanotti failure criterion utilises two different indices for fiber failure, previously reported in Eq. (3.49) and (3.50). Since both correspond to the same damage mechanism of fiber breakage, the failure damage variable is calculated for both and the maximum value is taken, Eq. (3.71), (3.72) and (3.73)[3].

$$d_{ft}^{f} = 1 - \frac{1}{\Phi_{ft}} \exp\left(\frac{(1-\Phi_{ft}) C_{11} L_c \left(\varepsilon_{11}^{fT}\right)^2}{G_{fc}^{T}} \right) \tag{3.71}$$

$$d_{fc}^{f} = 1 - \frac{1}{\Phi_{fc}} \exp\left(\frac{(1-\Phi_{fc}) C_{11} L_c \left(\varepsilon_{11}^{fC}\right)^2}{G_{fc}^{C}} \right) \tag{3.72}$$

$$d_{f}^{f} = \begin{cases} \sup_{\tau \leq t} \left(\max\left(d_{ft}^{f}, d_{fc}^{f} \right) \right), & \max\left(d_{ft}^{f}, d_{fc}^{f} \right) < 1 \\ 1, & \max\left(d_{ft}^{f}, d_{fc}^{f} \right) \geq 1 \end{cases} \tag{3.73}$$

Where G_{fc}^{T} and G_{fc}^{C} are the fracture toughnesses of the fiber under tension and compression respectively.

3.7 Material properties

In this study, the composite used is M49/42%/200T2X2/CHS-3K, which incorporates M49 epoxy resin with a 42% content in the composite material and CHS-3K carbon fibers arranged in a 0/90 orientation with a 2x2 twill weave. The composite is characterized by 26 layers, each with a thickness of 0.19 mm, and a density of 1.47 g/cm^3. The initial properties used to model this material with VUMAT are listed in table 3.1

Property	**Value**	**Unit**	**Source**
E_1	68000	MPa	Datasheet
E_2	68000	MPa	Datasheet
E_3	10000	MPa	Assumed from report[36]
G_{12}	5000	MPa	Assumed from report[36]
G_{13}	3500	MPa	Assumed from report[36]
G_{23}	3500	MPa	Assumed from report[36]
ν_{12}	0.03		Assumed from report[36]
ν_{13}	0.4		Assumed from report[36]
ν_{23}	0.4		Assumed from report[36]
ε_{11}^{fT}	0.015441176		Datasheet
ε_{22}^{fT}	0.015441176		Datasheet
ε_{33}^{fT}	0.02		Assumed from experimental data
$\lvert\varepsilon_{11}^{fC}\rvert$	0.015441176		Datasheet
$\lvert\varepsilon_{22}^{fC}\rvert$	0.015441176		Datasheet
$\lvert\varepsilon_{33}^{fC}\rvert$	0.05		Assumed from experimental data
γ_{12}^{f}	0.075		Assumed from experimental data
γ_{13}^{f}	0.05		Assumed from experimental data
γ_{23}^{f}	0.05		Assumed from experimental data
X_T	1050	MPa	Datasheet
X_C	730	MPa	Datasheet
Y_T	1050	MPa	Datasheet
Y_C	730	MPa	Datasheet
S_L	95	MPa	Assumed from experimental data
S_T	65	MPa	Assumed from experimental data
α_0	50	deg	Assumed from experimental data
β	1.000000E-05		Assumed from experimental data
G_{fc}^{T}	100	N/mm	Assumed from experimental data
G_{fc}^{C}	50	N/mm	Assumed from experimental data
$G_{mc}^{T} = G_{Ic}$	0.5	N/mm	Assumed from experimental data
G_{mc}^{C}	1.5	N/mm	Assumed from experimental data
$G_{mc}^{C} = G_{IIc}$	2.5	N/mm	Assumed from experimental data
η	0.0001		Assumed from experimental data
In-situ configuration	0		Assumed
t	0.19	mm	Datasheet
η_T	0		Assumed from experimental data
η_L	0		Assumed from experimental data
Θ_0	0	deg	Test dependent
$\chi = E_1^C/E_1$	1		Assumed
Diffuse damage model			Test dependent
Strain fail	0.3		Assumed

Table 3.1: Material properties VUMAT

Chapter 4

Experimental analysis

4.1 Experimental test

The experimental part of this study aims to determine the erosion rate of the examined plate by varying the angle of impingement and the test duration. The duration of the tests was initially defined by conducting an experiment on a specimen inclined at 60°, an angle known from the literature to be associated with the maximum erosion rate. The specimen was subjected to erosion until a complete perforation occurred, which was observed after 3 minutes. Based on this result, test durations of 30, 75, and 120 seconds were selected. The conducted tests are summarized in table 4.1.

Case	**Angle of Impingement**	**Period (s)**
1	30°	30
2	30°	75
3	30°	120
4	60°	30
5	60°	75
6	60°	120
7	90°	30
8	90°	75
9	90°	120

Table 4.1: Erosion test cases

The test bench used to perform the tests is shown in the figure 4.1. It consists of a funnel to contain the sand, a strain sensor attached to it to measure the mass of sand ejected over the considered time period, a blasting gun connected to a compressor ensuring a pressure of 6 *bar* and a calibrated knob attached to the specimen holder, that allows measuring the angle between the sample and the sand jet.

Figure 4.1: Test bench

In order to calculate the mass eroded by the sand particles, each specimen was weighed before and after the test using an electronic balance with a sensitivity of 0.01 mg, Figure 4.2. Each specimen was weighed five times, and the average value was considered.

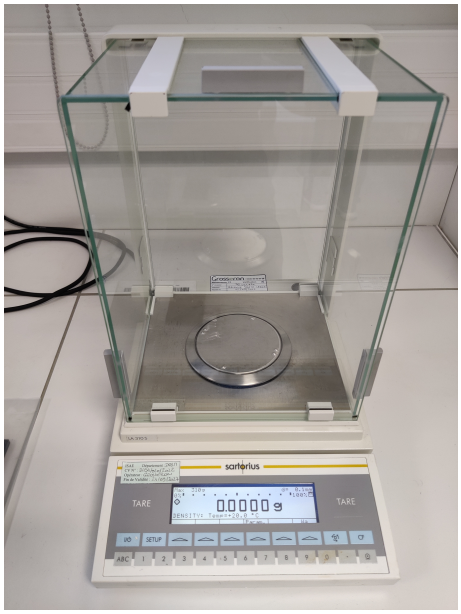

Figure 4.2: Precision balance

Each test was carried out by first starting the recording of the mass variation, performed using a computer connected to the sensor. The compressed air jet was then activated through the nozzle simultaneously with the start of the timing, which

was simply monitored using a mobile phone stopwatch. At the end of the predefined time, the specimen was disassembled, rinsed with water, and dried using compressed air and absorbent paper. As previously described, the specimen was then weighed. This procedure was repeated for each test.
The specimen masses, measured before and after each test, are reported in the Figures 4.3 and 4.4. The results obtained and their discussion are presented in the dedicated chapter.

BEFORE TESTS						
Specimen	Value 1 [g]	Value 2 [g]	Value 3 [g]	Value 4 [g]	Value 5 [g]	Mean value [g]
1	58.9774	58.9775	58.9775	58.9774	58.9774	**58.97744**
2	58.5513	58.5512	58.5513	58.5513	58.5513	**58.55128**
3	58.4919	58.4919	58.492	58.4919	58.492	**58.49194**
4	58.6938	58.6938	58.694	58.6938	58.6939	**58.69386**
5	58.9427	58.9428	58.9428	58.9427	58.9427	**58.94274**
6	59.106	59.1058	59.1058	59.1059	59.1058	**59.10586**
7	58.7599	58.7599	58.76	58.76	58.76	**58.75996**
8	58.8019	58.8019	58.8019	58.8018	58.8018	**58.80186**
9	59.2012	59.2013	59.2014	59.2012	59.2012	**59.20126**

Figure 4.3: Specimen mass measurements before the tests

AFTER TESTS						
Specimen	Value 1 [g]	Value 2 [g]	Value 3 [g]	Value 4 [g]	Value 5 [g]	Mean value [g]
1	58.9277	58.9276	58.9276	58.9277	58.9278	**58.92768**
2	58.4293	58.4293	58.4292	58.4291	58.4292	**58.42922**
3	58.2558	58.2558	58.2558	58.2556	58.2557	**58.25574**
4	58.6017	58.6016	58.6017	58.6016	58.6017	**58.60166**
5	58.7257	58.7256	58.7255	58.7255	58.7256	**58.72558**
6	58.7523	58.7524	58.7523	58.7521	58.7523	**58.75228**
7	58.6701	58.67	58.67	58.6701	58.6702	**58.67008**
8	58.6002	58.6002	58.6001	58.6002	58.6001	**58.60016**
9	58.8949	58.8947	58.8949	58.8949	58.8948	**58.89484**

Figure 4.4: Specimen mass measurements after the tests

Chapter 5

Numerical model

5.1 Sand modeling

As discussed in the chapter on the state of the art, an important factor influencing erosion is the shape of the erosive particles. For this reason, a characterization of the particles was carried out.
The granulometry has been measured by a laser granulometry process to measure the diameter of the particles. This sand used for the erosion of the composite plate has a particle size distribution shown in the figure 1.2, where "particle diameter" refers to the largest dimension of the particle. This study was conducted by the Clément Ader Institute.
The need to obtain a realistic particle model arises not only because erosion itself is influenced by particle shape but also to ensure that the erosion pattern of the surface reflects the realistic trend observed in the experimental tests.
For this scope were taken photographs of 25 sand grains using the scanning electron microscope shown in figure 5.1.

Figure 5.1: Electron microscope

This allowed for the measurement of the width and length of each individual particle. The height could only be determined for five particles, as it was not possible to find a stable resting point for the remaining ones to obtain a proper microscope image. For these five particles, the ratio of the height to their shortest side provided a set of values, the average of which was calculated. This average value, equal to 0.72, was then used to estimate the height of the remaining particles by multiplying it by their shorter side. Thus, the height, width and depth of each individual particle have been defined, Table 5.1.

Particle	**Length** $[mm]$	**Width** $[mm]$	**Height** $[mm]$
1	731	368	264
2	1162	607	416
3	670	488	351
4	761	488	351
5	738	535	384
6	589	444	319
7	670	394	284
8	710	508	553
9	794	570	356
10	714	650	437
11	620	423	315
12	608	433	349
13	462	406	292
14	688	625	375
15	603	414	299
16	498	398	286
17	733	594	500
18	713	637	465
19	326	306	220
20	647	413	297
21	569	489	293
22	905	639	365
23	638	382	275
24	488	439	296
25	535	346	328

Table 5.1: Particle measurements

The graph 5.2 shows the size distribution of the large garnet particles in terms of percentage proportion to their diameter, showing a distribution similar to that obtained through the laser particle size process. Therefore, it can be concluded that the randomly selected particles are representative and can be used for the desired simulation.

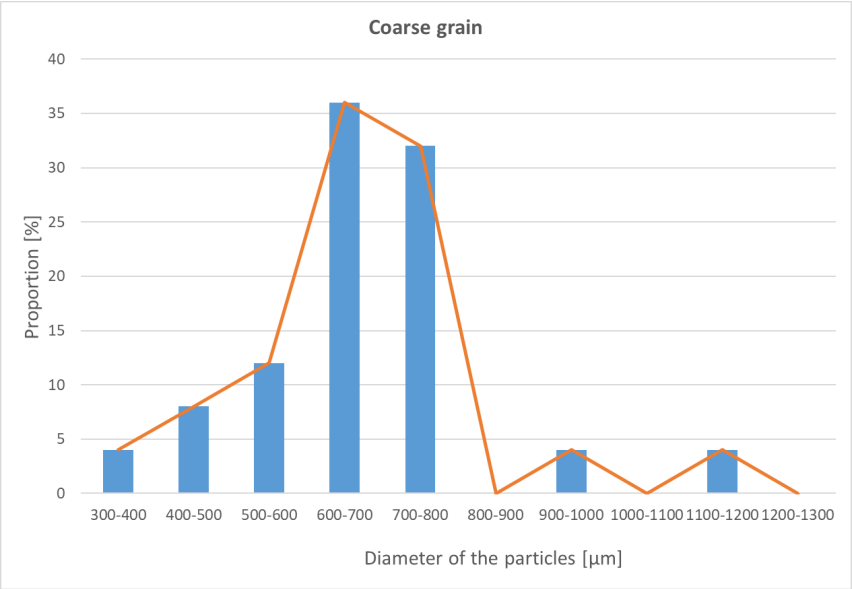

Figure 5.2: Particle diameter distribution

An image of a selected particle is provided, which will be used as an example in the following section, figure 5.3.

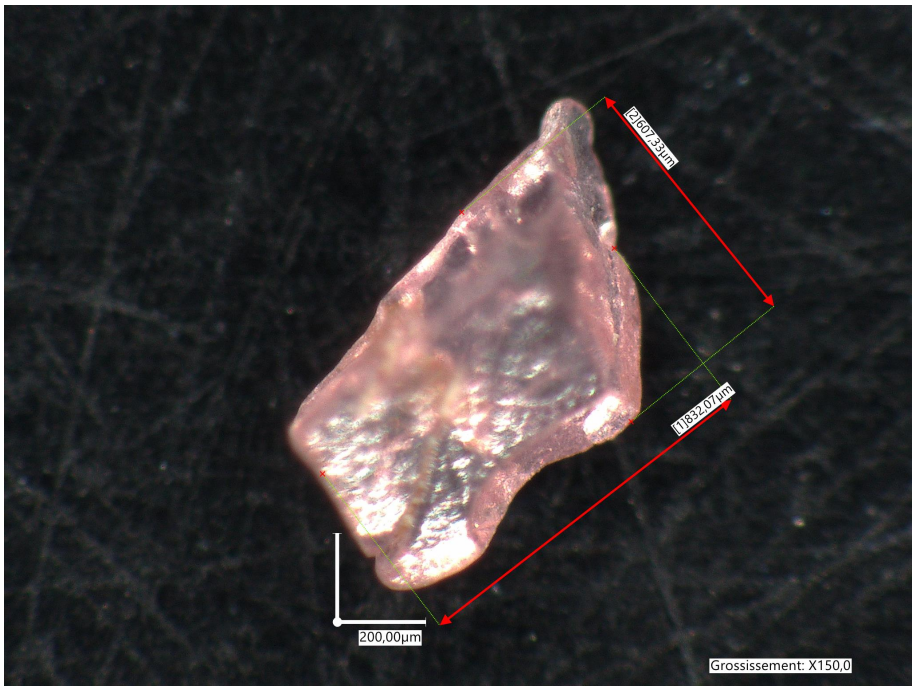

(a) Particle width and length

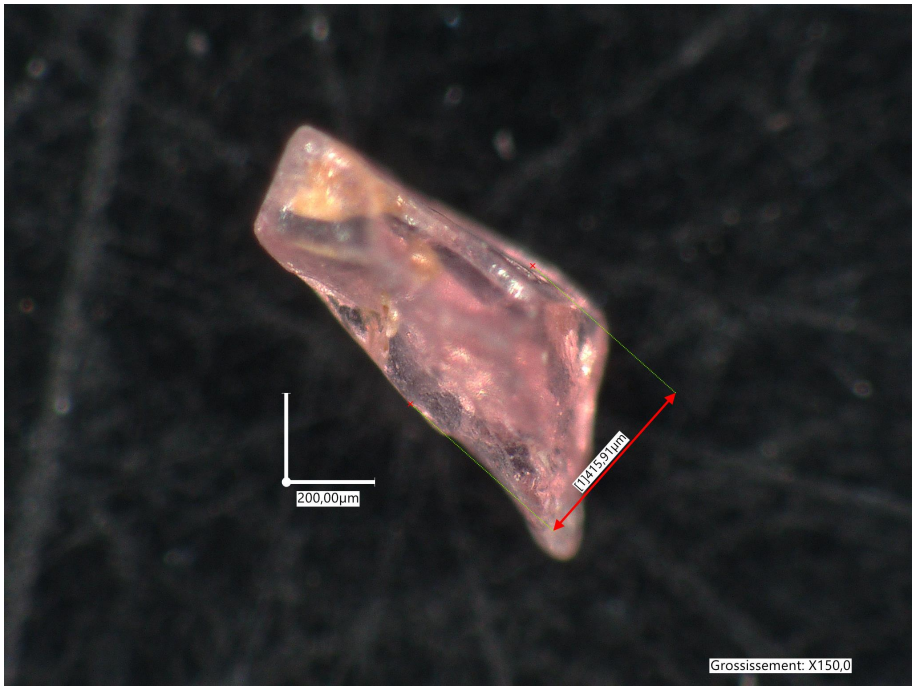

(b) Particle height

Figure 5.3: Measure of particle

The obtained images are processed using a MATLAB program to generate a three-dimensional representation of the particle that is as realistic as possible. Since image processing involves a conversion to grayscale and then to a binary scale, particle images with poorly defined edges due to their light color could not be used. As a result, 23 particles were successfully modeled. From these binary images the costum MATLAB script extracts the contour of the loaded particle. If it is not extracted

optimally, it is possible to manually intervene by specifying the points that do not belong to the contour so that MATLAB forms the contour without using them, Figure 5.5.

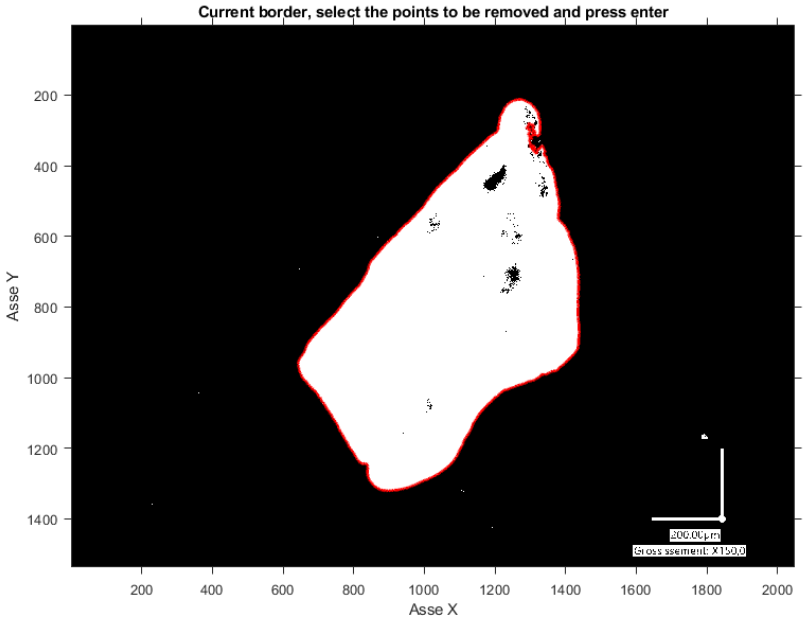

(a) Selection of excessive points

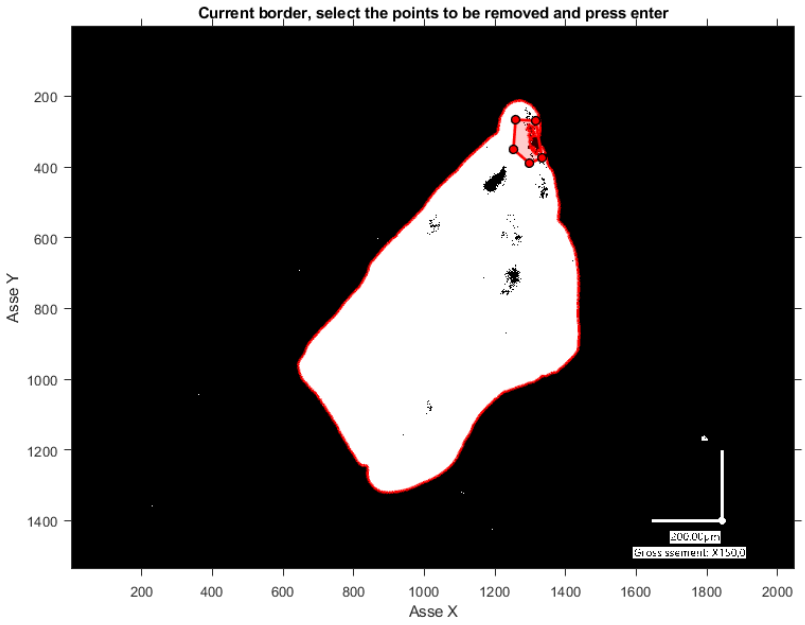

(b) Process obtaining optimal edge

Figure 5.4: Process obtaining optimal edge

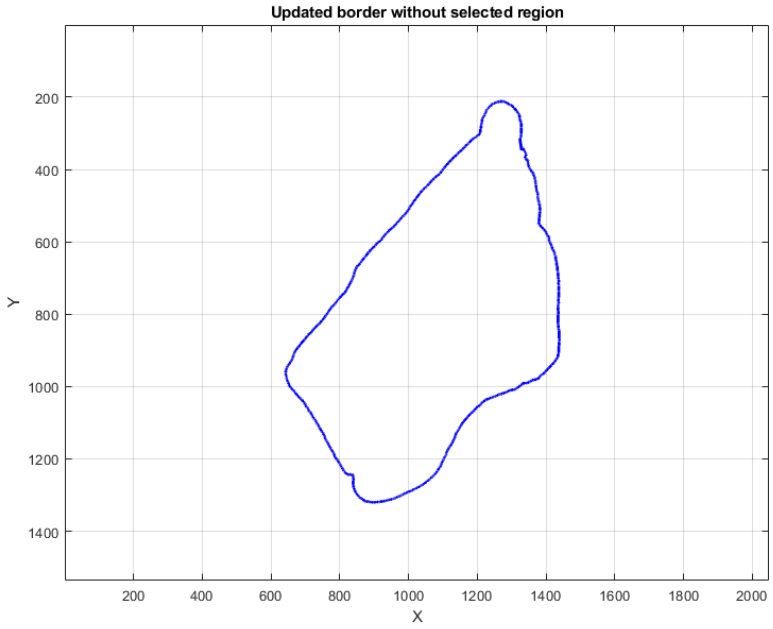

(c) Edge updated

Figure 5.5: Process obtaining optimal edge

By providing the particle's height and the desired number of layers as input, the program automatically divides the height by the specified number of layers.
For each layer, the user is asked to manually draw the contour, which is then used for the 3D modeling process from the initial images of the particles. These were interpolated using the same number of points as those used to interpolate the base edge, the edge extracted by MATLAB, to generate the .stl file, which is explained later. Using the previously represented particle, the figure 5.6 illustrates how the contours for each selected layer were obtained. The red contour represents the one extracted by MATLAB, while the blue contours are manually drawn by the user. These were then mirrored respect the base plane.

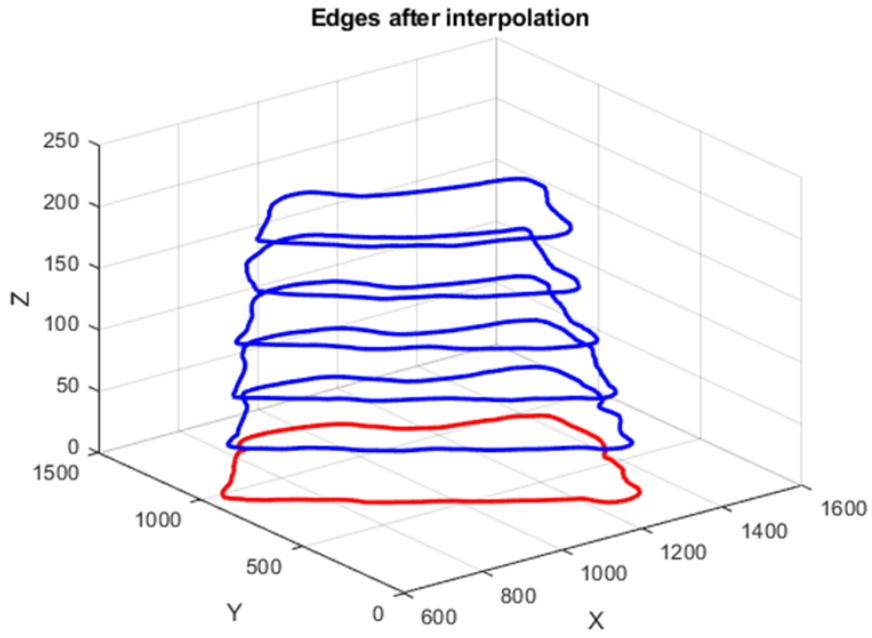

Figure 5.6: Edges particle

The obtained contours were located in a matrix, pairing each with its successive contour. From these matrices, the geometric representation of the surfaces between two consecutive contours was extracted using a face-vertex representation. This representation was then processed to generate a triangular mesh of the particle's surface. This process resulted in a 3D representation of the particle, which was saved in an .stl file.
This type of file is not readable by Abaqus. Therefore, it was processed using SolidWorks to generate a .step file. Using this software, the moments of inertia and the volume of the particles were also calculated. Their masses were determined by assigning them a density of 1000 kg/m^3, different from that previously reported because it must take into account the space occupied by air in calculating volumetric density.
The obtained 3D model of the sample particle is shown in figure 5.7. By comparing it with the reference image, it can be observed that the particle's edges and measures have been accurately preserved, resulting in a high-quality three-dimensional model. This process was repeated for each particle photographed, resulting in a total of 23 3D models.

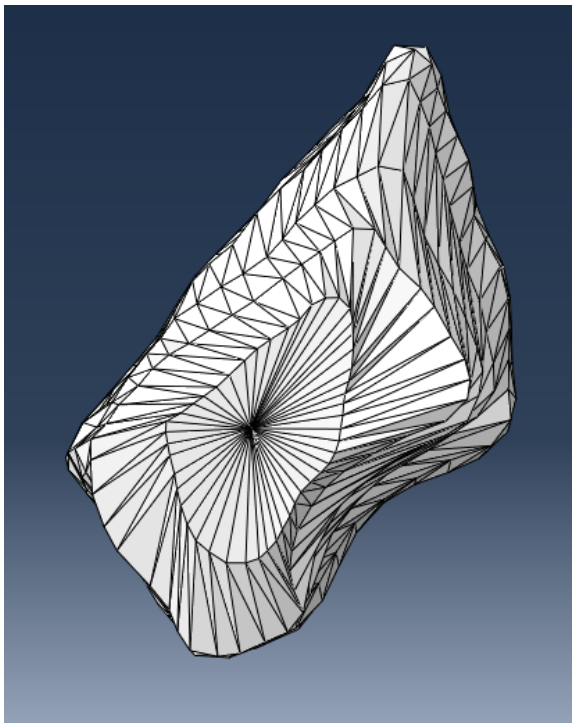

Figure 5.7: 3D particle on Abaqus

5.2 FEM model

The objective of this project is to simulate the erosion behavior of a composite plate subjected to the impact of sand particles. The plate consists of 26 layers, each 0.19mm thick. Each layer consists of 2x2 twill carbon fibers immersed in an M49 epoxy resin. Mechanical characteristics provided by the datasheet, are shown in Table 5.2.

Property	**Details/Methods**	**Value**	**Units**
General Material Properties			
Fibre	HS Carbon	-	-
Tow	3K	-	-
Weave	Twill 2x2	-	-
Mass	-	200	g/m^2
Nominal Cured Ply Thickness	-	0.235	mm
Nominal Fibre Volume	-	47.8	%
Nominal Laminate Density	-	1.47	g/cm^3
Mechanical Properties			
Tensile Strength	Carbon EN2561	1050	MPa
Tensile Modulus	Glass EN2747	68	GPa
Flexural Strength	Carbon EN2562	1000	MPa
Flexural Modulus	Glass EN2746	60	GPa
ILSS (Interlaminar Shear Strength)	Carbon EN2563 / Glass EN2377	60	MPa
Compression Strength	EN2850 B	730	MPa

Table 5.2: Properties of composite material

5.2.1 Parts modelling

Each modeled particle was imported into Abaqus via the .step file as a Discrete Rigid 3D Body. To simplify the model and reduce computational time, the internal parts of the particles were removed. This operation was also performed considering the rigidity assumption assigned to the particles, as their deformations were deemed negligible for the analysis. As previously mentioned, each particle was assigned a mass and moments of inertia, using a density of 1000 kg/m^3. Additionally, each particle was given a velocity of 150 m/s, a value obtained through high-speed camera measurements.
To further reduce computational time, only a portion of the specimen was modeled. The specimen was created from a sketch 15 x 15mm with a depth of 4.94 mm, defined as a 3D deformable body.
Since the model is analyzed using the VUMAT subroutine, it was necessary to partition the plate for each individual layer. The material was then assigned to the plate using the 40 constants required for its definition, as previously shown in figure 5.2. To simulate the real-world clamping conditions of the plate, all degrees of freedom were constrained at the final layer. The sample obtained is shown in Figure 5.8.

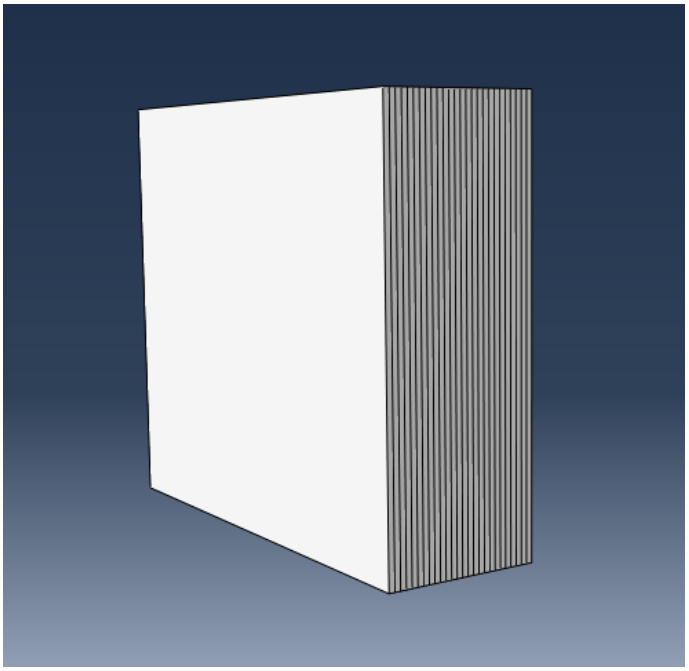

Figure 5.8: Sample

5.2.2 Assembling

In reality, the distance between the nozzle of the compressed air gun and the specimen is 25 mm. However, since the interaction between air and particles is not considered in this study, this parameter does not affect the results obtained in Abaqus. Therefore, the complete model was created without including this parameter, and the assembly was designed by minimizing the distance between the particles and the sample to reduce computational time. Given the high-quality particle modeling, a

repetition of the same particles was used in the simulations.
The interaction between the particles and the plate was simulated, while the interaction between the particles themselves was not considered, again to reduce computational time. This interaction was modeled using a general contact approach, with the assigned property defined as IntProp-1, which has the following characteristics:

- In the normal direction, a Hard contact behavior was assigned to prevent interpenetration. Additionally, the option allowing for surface separation at the particle-plate interface was enabled to ensure the correct detachment behavior after contact;
- A tangential behavior with a friction coefficient of 0.33 and isotropic directionality.

5.2.3 Mesh

For the particle mesh, elements of type R3D4 or R3D4 were used, where the abbreviation is as follows: R because they are rigid elements, $3D$ three dimensional analysis and the last number is the number of nodes. For the sample, elements of type C3D8 that is an 8-node linear brick element were used, with a finer mesh at the center of the plate, where elements of 50 micrometers were placed, gradually expanding towards its edges, Figure 5.9.

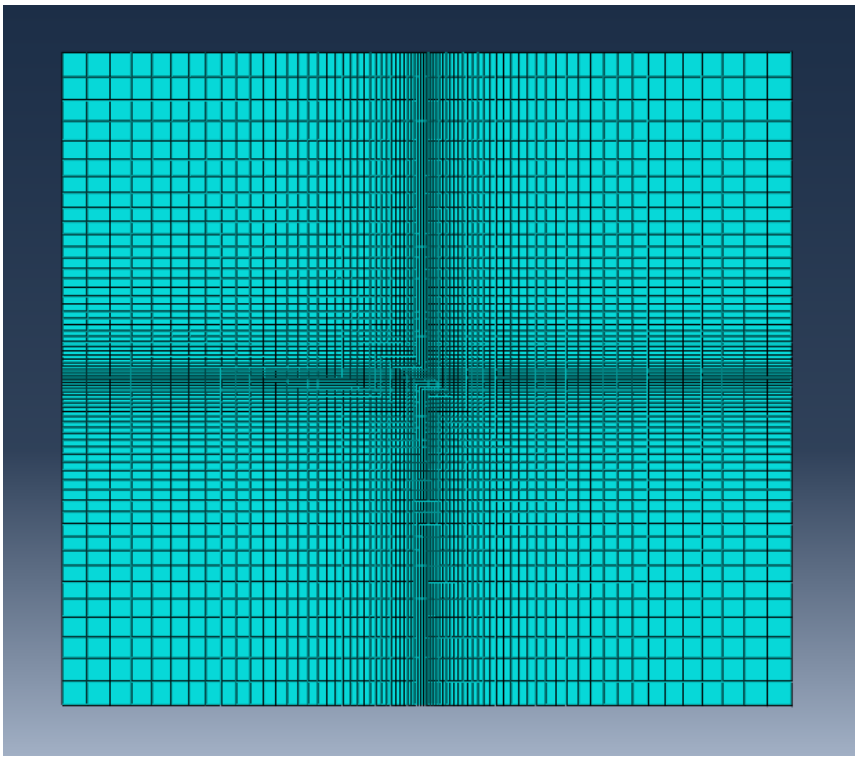

Figure 5.9: Mesh sample

The model has been defined in its entirety and is shown in Figure 5.10

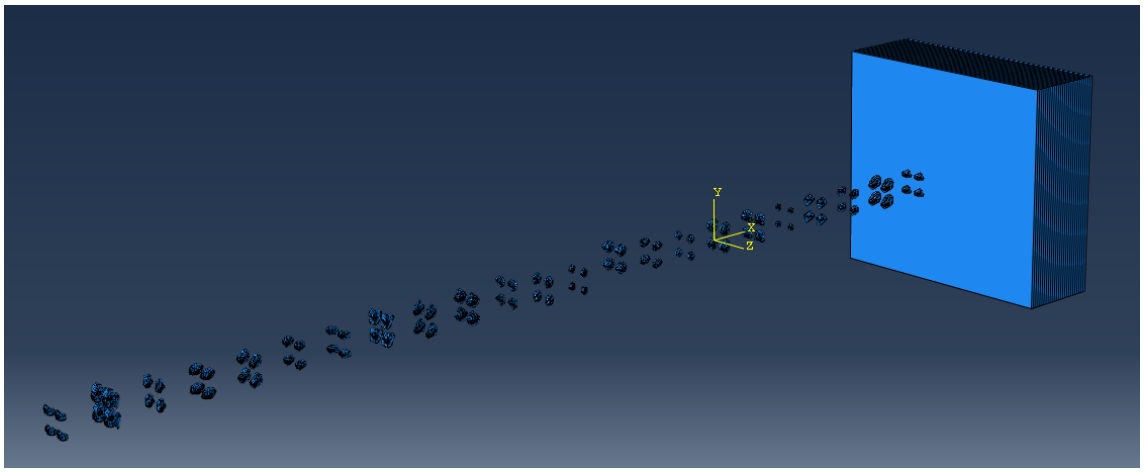

Figure 5.10: complete model

5.2.4 Hypothesis

From the Table 4.1, it can be observed that the minimum duration of the experimental tests is 30 seconds. From the calculation of the mass of the analyzed particles, an average value of $63.2 \cdot 10^{-6}$ g is obtained. Furthermore, from the graphs of the variation in the weight of the sand contained within the funnel, measured using the sensor, Figure 5.11, an average flow rate of 7.6 g/s is found. This results in a flow of 120 particles per millisecond, not considering their interaction.

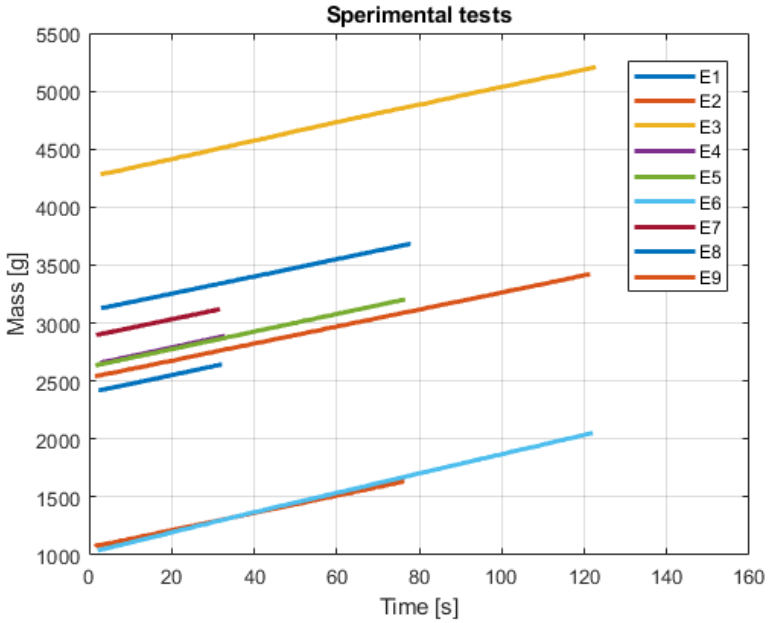

Figure 5.11: Particle mass flow

This makes impossible to simulate the entire duration of the tests through numerical analysis. The fundamental assumption is therefore to simulate the same particle flow per second but using a scaling factor for the simulated time. This factor was calculated by comparing the impact area obtained in the experimental tests with that of the numerical simulations.

In particular, the circular impact area was calculated assuming that the beam opening angle was equal to 15°, obtained through the analysis of image 5.12, captured using a high-speed camera, from a previous study by Ph.D. Candidate Adrien Sapet [37] using a nozzle with a diameter of 4 mm.

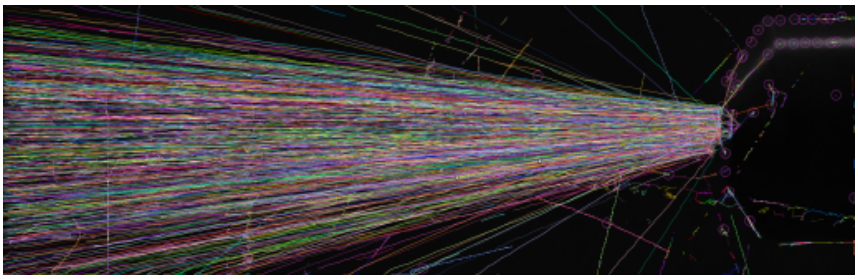

Figure 5.12: Tracked sand flow

The test bench used is equipped with a nozzle with a diameter of 7 mm.
Based on these data, the real impact surface was calculated to be 326.77 mm^2, which was then compared to the simulated impact surface of 115 mm^2, which was calculated by considering the frontal area of the impacting particles, figure 5.13, resulting in a time scaling factor of 110.

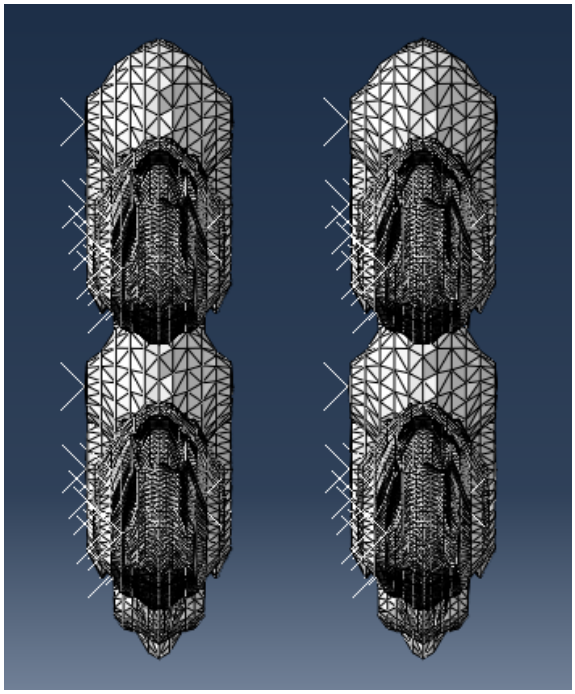

Figure 5.13: Impact surface Abaqus model

Chapter 6

Analysis and results

6.1 Sperimental tests

The photographs of the specimen morphology after being subjected to tests of the same duration, namely 2 minutes, but with increasing impact angles of 30°, 60°, and 90°, are reported in Figures 6.1 and 6.2. The observed behaviors align with those reported in the literature.
In particular, as the impact angle increases, there is a transition from a higher presence of cuts on the matrix to its removal, along with an increasing occurrence of random fiber fracturing at high impact angles, which leads to the loss of their original orientation.
At low impact angles, since the tangential force plays a significant role, the damage occurs primarily through micro-cutting and micro-ploughing. Conversely, at high impact angles, the tangential force becomes negligible and ultimately vanishes at 90°, while the normal force becomes dominant, leading to micro-cracking of both the matrix and the fibers.

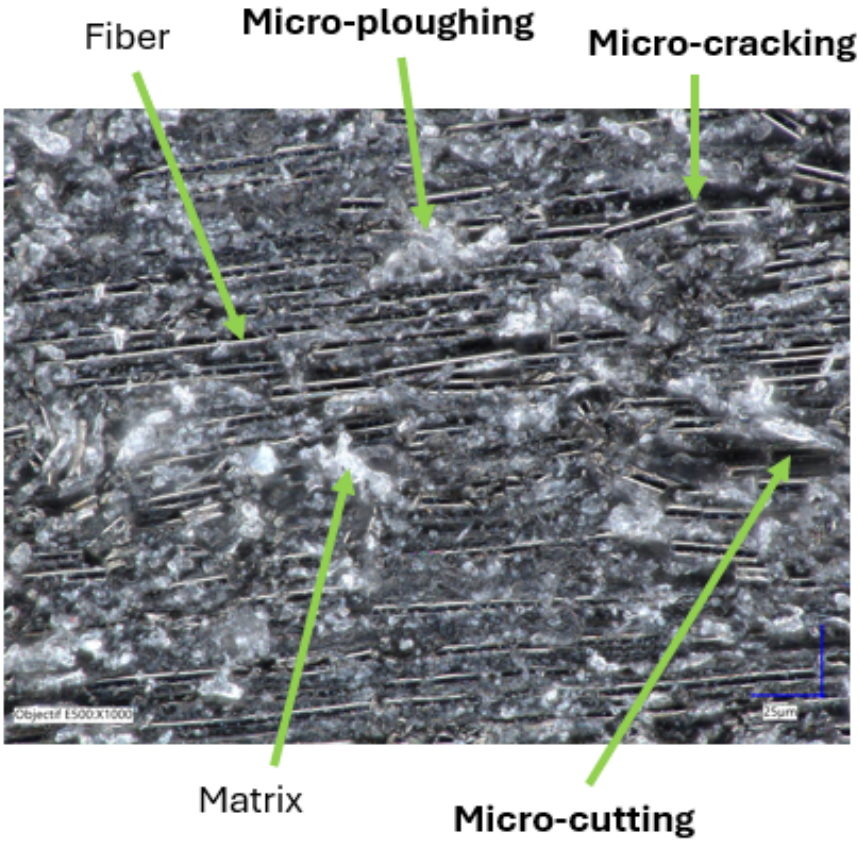

(a) **Case E3:** impact angle 30° time 120s

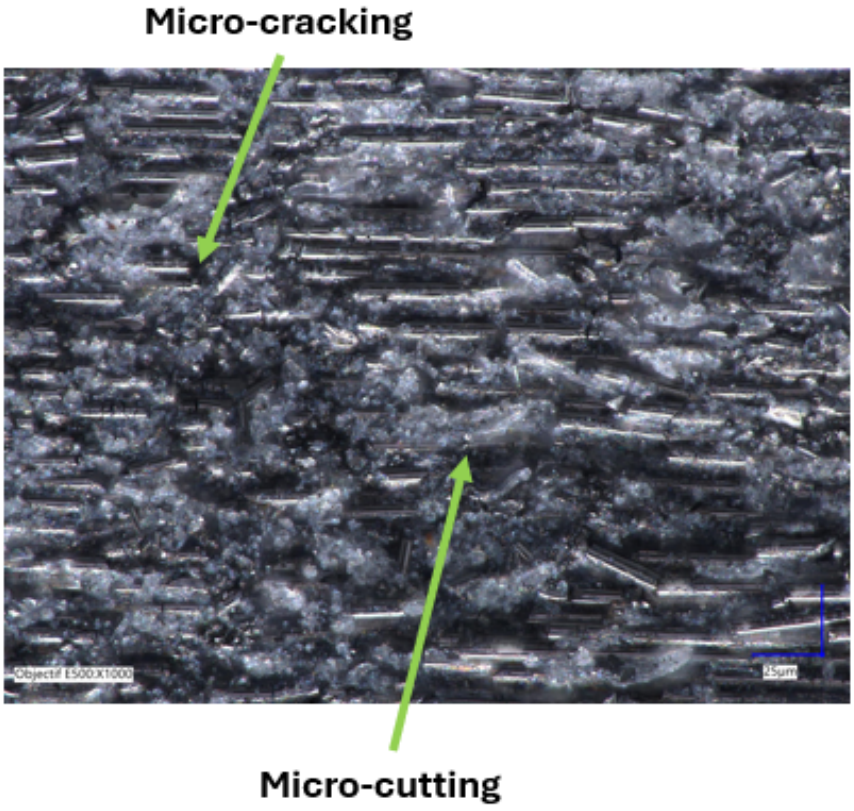

(b) **Case E6:** impact angle 60° time 120s

Figure 6.1: Samples morphology after test

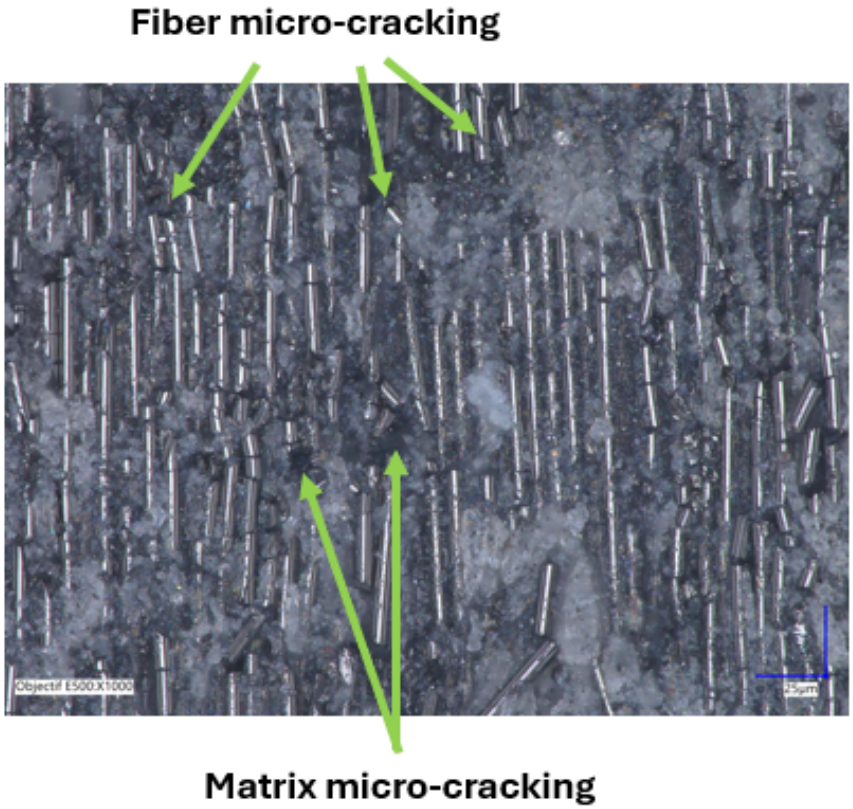

(c) **Case E9:** impact angle 90° time 120s

Figure 6.2: Sample morphology after test

From the performed tests, the values of eroded mass reported in the Table 6.1 were obtained.

Case	Eroded mass [g]
E1 30 deg 30 sec	0.04976
E2 30 deg 75 sec	0.12206
E3 30 deg 120 sec	0.2362
E4 60 deg 30 sec	0.0922
E5 60 deg 75 sec	0.21716
E6 60 deg 120 sec	0.35358
E7 90 deg 30 sec	0.08988
E8 90 deg 75 sec	0.2017
E9 90 deg 120 sec	0.30642

Table 6.1: Eroded mass for different test cases

These values were then plotted on the graph 6.3, which shows the eroded mass of the specimen as a function of the test duration, fixing the angle of impact for the single curve, it can be observed that the experimentally obtained results are perfectly in

line with those reported in the literature. The highest eroded mass is obtained in the case of a 60° impact angle, followed by the case where the flow is perpendicular to the plate, and lastly, the case with a 30° impact angle.

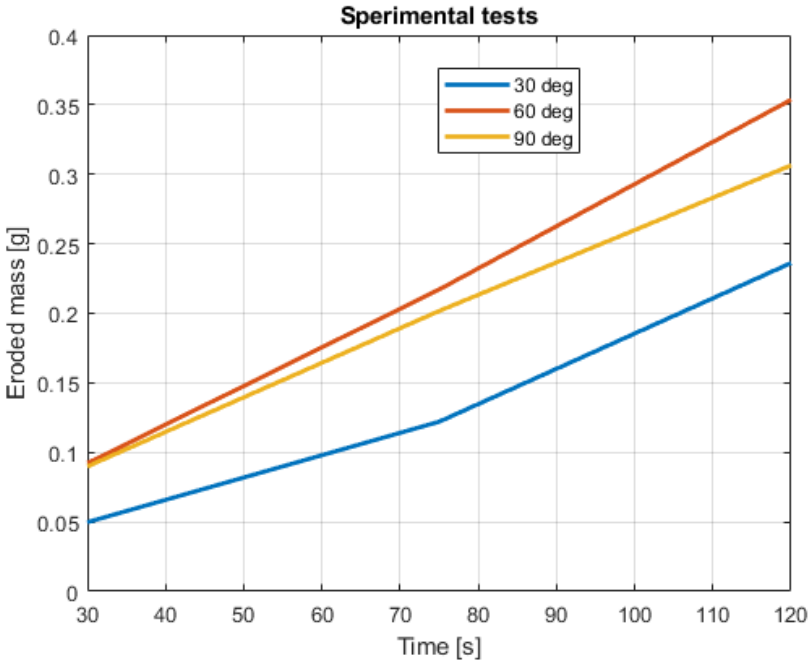

Figure 6.3: Time-dependent eroded mass

Different erosion rate values were thus obtained, as reported in Table 6.2. These values will be compared with the erosion rates obtained from the simulation.

Impact angle [deg.]	**Erosion rate [g/s]**	**Erosion rate [g/s]**	**Mean [g/s]**
30	0.001606667	0.002536444	0.002071556
60	0.002776889	0.003031556	0.002904222
90	0.002484889	0.002327111	0.002406000

Table 6.2: Erosion rate for different impact angles

6.2 Numerical Analyses

Analyses were conducted to examine how the selected diffuse damage model, chosen between Wang's model and the Expanded model could influence the analysis.
The images 6.4 show the study of the influence of the adopted diffuse damage model. The use of the Wang's model results in a lower maximum stress within the plate compared to the expanded model. The expanded model was chosen for this study as it provides a more detailed representation of the coupling between the principal stress directions.

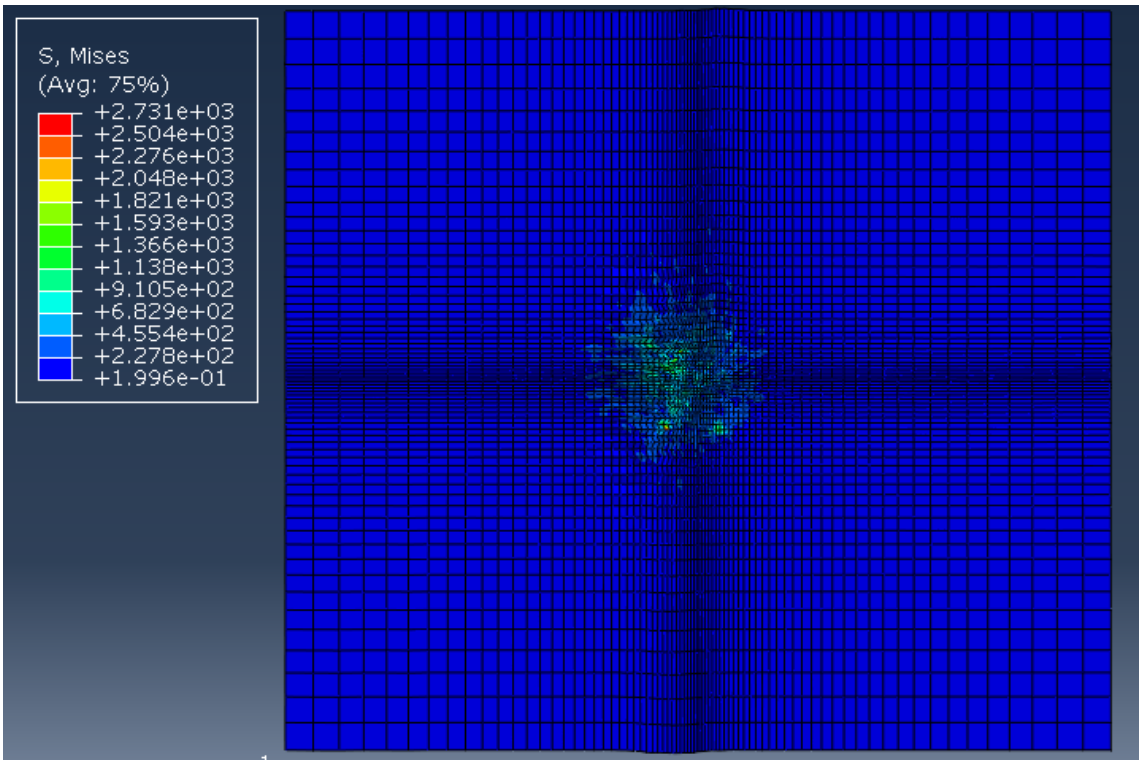

(a) Wang's diffuse damage model

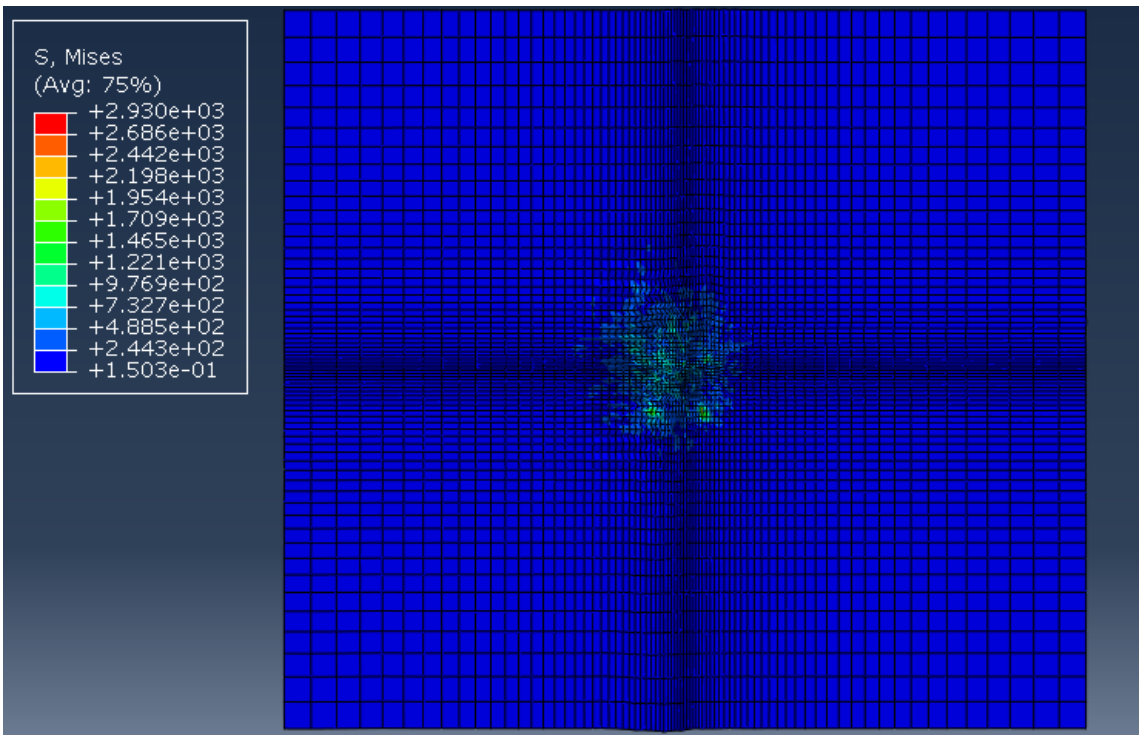

(b) Expanded diffuse damage model

Figure 6.4: Influence of the adopted diffuse damage model

After defining all the parameters on the VUMAT, simulations were performed for three different impingement angles: 90°, 60°, and 30°, reported in the following figures.

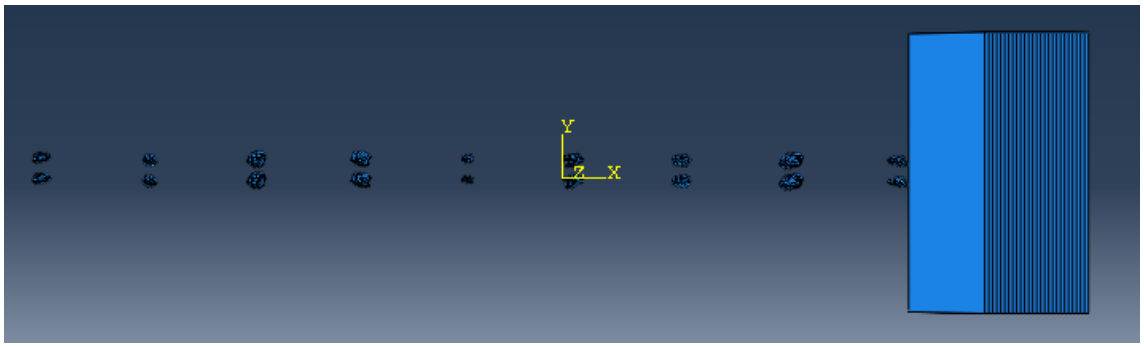

Figure 6.5: 90° perspective model

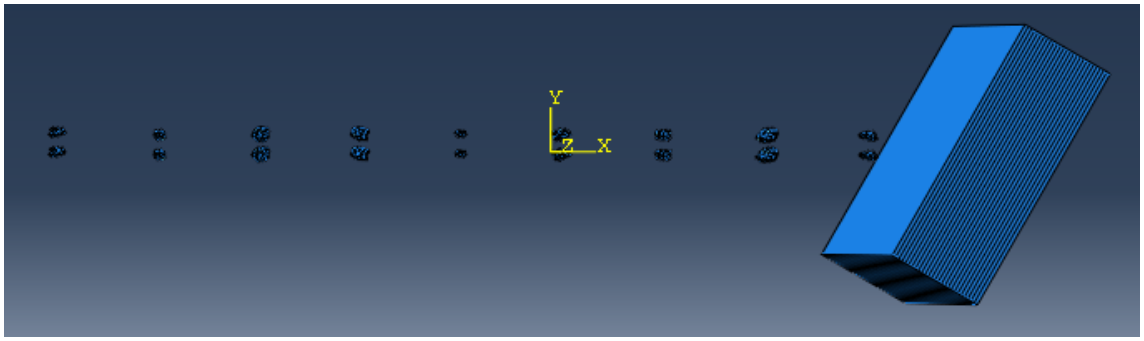

Figure 6.6: 60° perspective model

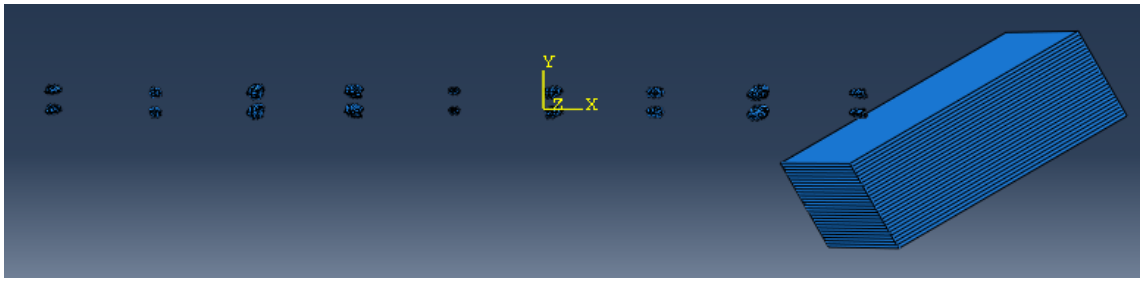

Figure 6.7: 30° perspective model

The simulated time reaches a value of 0.22 s, using the previously mentioned scaling factor.
From the results obtained, Table 6.3, where the erosion rate values for each individual step and their average are reported, and Figure 6.8, can be observed that the model successfully simulates the erosion rate value, especially in the case where the specimen is positioned at 90°. However, it does not perfectly replicate the trend of the composite material under study, which exhibits greater erosion at an impact angle of 60°.

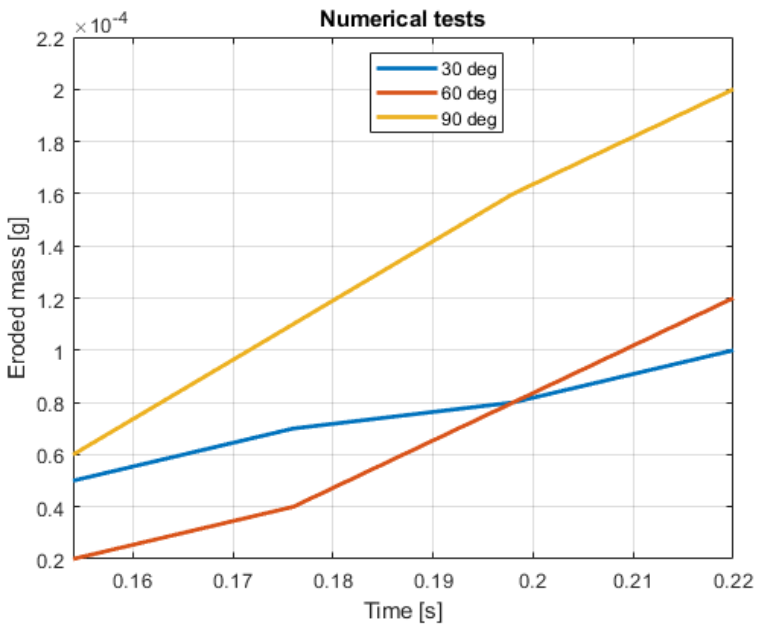

Figure 6.8: Time-dependent eroded mass model

Impact angle [deg.]	**Erosion rate [g/s]**	**Mean [g/s]**
90	0.00227 0.00227 0.00181	0.00212
60	0.00090 0.00181 0.00181	0.00151
30	0.00090 0.00045 0.00090	0.00076

Table 6.3: Erosion rates from numerical simulations at different impact angles.

On the other hand, if we observe the trend of the eroded mass in the experimental tests as a function of the impact angle, while keeping the test duration fixed for each curve, Figure 6.9, it becomes evident that as the test duration decreases, the peak value at 60° also decreases.

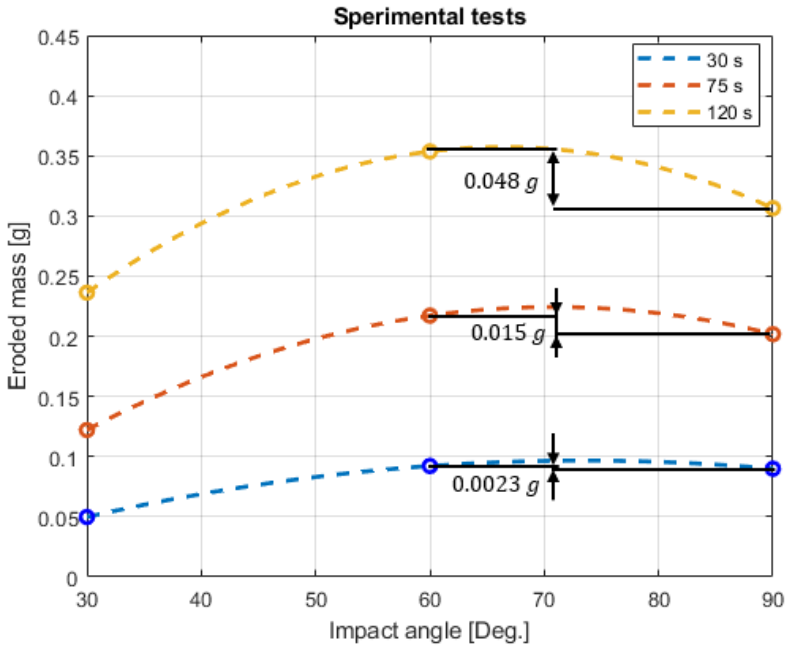

Figure 6.9: Effect of impact angle on eroded mass at different exposure times

This suggests that as the test duration shortens, the eroded mass at an impact angle of 60° decreases compared to that at 90°. Consequently, this would make the numerical model perfectly consistent with the experimental results.

Chapter 7

Conclusions and future developments

Helicopters often operate in extreme environments where a two-phase flow, air mixed with solid particles like sand, is present. These particles interact with moving components, causing erosion that shortens operational lifespan and increases maintenance needs.
This study begins with an analysis of erosion phenomena and the factors influencing them. In accordance with definitions found in the state of the art, the erosion rate is defined as the ratio between the mass loss of the eroded material and the mass of the impacting particles.
The erosion rate of the material depends on several factors, such as the impact angle and the shape of the particles. The impact angle, the angle between the trajectory of the particle and the surface, is a key parameter. At low angles ($15° - 30°$), ductile materials exhibit higher erosion due to micro-cutting and ploughing. In contrast, brittle materials show maximum erosion at 90° due to fibers and matrix micro-cracking. Notably, in composites with brittle fibers like carbon or glass in an epoxy matrix, the erosion peak shifts to 60°.
In the second part of the study, a sand particle model was developed to create a numerical simulation capable of replicating, as accurately as possible, the real behavior of the specimen. The specimen is made of composite material structured in 26 layers, each composed of [0,90] carbon 2x2 twill fibers embedded in M49 epoxy resin. It was subjected to tests at impact angles of 30°, 60°, and 90°, with durations of 30 s, 75 s, and 120 s.
Sand characterization was based on a sample with a bulk density of 2330 kg/m^3.For the simulations, a reduced density of 1000 kg/m^3 was assumed. This value was lowered to account for the voids occupied by air within the material. Electron microscope images of 23 particles were processed, and their size distribution was compared with laser granulometry results, showing good agreement. The 3D shapes were reconstructed using MATLAB, allowing users to outline cross-sectional layers. The models were finalized in SolidWorks for integration into Abaqus. In particular, the model developed in Abaqus uses the VUMAT subroutine created by Professor Lachaud at ISAE-SUPAERO, with the aim of laying the groundwork for its validation in the study of the erosion phenomenon.

Results from experimental tests at 30°,60°, and 90° confirmed literature trends: low angles result in micro-ploughing and micro-cutting of matrix, while higher angles lead to matrix removal and fiber cracking. The highest erosion was observed at 60°,

consistent with previous studies on composite materials.
The erosion rate values obtained from the numerical simulations for impact angles of 30°, 60°, and 90° are similar to those measured in the experimental tests. However, the maximum erosion rate is observed at 90°, unlike in the experiments where it occurs at 60°, this discrepancy may result from the test duration: shorter tests tend to reduce the peak at 60°, aligning better with the simulation results.
It is necessary to determine if the previous conclusion is correct by conducting experimental tests of shorter duration, on the order of seconds, and measuring the eroded mass of the material. However, this would require a balance with sensitivity even higher than the used in this study. Thus, an alternative approach is suggested: seeking a simplification of the model to enable longer-duration tests that may better correspond to real conditions. This could be achieved by using particles with a simplified shape, such as ellipsoidal ones, figure 7.1, thereby sacrificing a more detailed simulation but ensuring that they maintain the same erosion capacity as those simulated in this study.

Figure 7.1: Elipsoidal particle

Bibliography

[1] Alberto Millazzo. *Corso di Materiali Aerospaziali*. Università degli studi di Palermo.

[2] N. Vijay, V. Rajkumara, and P. Bhattacharjee. "Assessment of Composite Waste Disposal in Aerospace Industries". en. In: *Procedia Environmental Sciences* 35 (2016), pp. 563–570. ISSN: 18780296. DOI: 10.1016/j.proenv.2016.07.041. URL: https://linkinghub.elsevier.com/retrieve/pii/S187802961630130X (visited on 03/04/2025).

[3] Luis Laborda Pérez. "Damage and failure identification of composite laminates with carbon fibers and thermoplastic matrix under static and dynamic loading". PhD thesis. ISAE Supaero, Aug. 2024.

[4] Erasmo Carrera. *Corso strutture aeronautiche*.

[5] R. Talreja and C. V. Singh. *Damage and Failure of Composite Materials*. Vol. Cambridge University Press. 2012.

[6] John A. Nairn. "Matrix Microcracking in Composites". In: (2000).

[7] Robert Livingston and Behrad Koohbor. "Characterizing fiber-matrix debond and fiber interaction mechanisms by full-field measurements". en. In: *Composites Part C: Open Access* 7 (Mar. 2022), p. 100229. ISSN: 26666820. DOI: 10.1016/j.jcomc.2022.100229. URL: https://linkinghub.elsevier.com/retrieve/pii/S2666682022000020 (visited on 02/25/2025).

[8] J.-C. Grandidier, G. Ferron, and M. Potier-Ferry. "Microbuckling and strength in long-fiber composites: theory and experiments". en. In: *International Journal of Solids and Structures* 29.14-15 (1992), pp. 1753–1761. ISSN: 00207683. DOI: 10.1016/0020-7683(92)90168-S. URL: https://linkinghub.elsevier.com/retrieve/pii/002076839290168S (visited on 02/25/2025).

[9] Thomas Keller and Martin Schollmayer. "Plate bending behavior of a pultruded GFRP bridge deck system". en. In: *Composite Structures* 64.3-4 (June 2004), pp. 285–295. ISSN: 02638223. DOI: 10.1016/j.compstruct.2003.08.011. URL: https://linkinghub.elsevier.com/retrieve/pii/S0263822303002356 (visited on 02/25/2025).

[10] Chao Zheng et al. "Numerical study of impact erosion of multiple solid particle". en. In: *Applied Surface Science* 423 (Nov. 2017), pp. 176–184. ISSN: 01694332. DOI: 10.1016/j.apsusc.2017.06.132. URL: https://linkinghub.elsevier.com/retrieve/pii/S0169433217317889 (visited on 02/10/2025).

[11] C. Hernandez et al. “A computational determination of the Cowper–Symonds parameters from a single Taylor test”. en. In: *Applied Mathematical Modelling* 37.7 (Apr. 2013), pp. 4698–4708. ISSN: 0307904X. DOI: 10.1016/j.apm.2012.10.010. URL: https://linkinghub.elsevier.com/retrieve/pii/S0307904X12006154 (visited on 02/07/2025).

[12] G. Cowper and P. Symonds. “Strain hardening and strain-rate effects in the impact loading of cantilever beams”. In: (1957).

[13] A.S. Milani et al. “An improved multi-objective identification of Johnson–Cook material parameters”. en. In: *International Journal of Impact Engineering* 36.2 (Feb. 2009), pp. 294–302. ISSN: 0734743X. DOI: 10.1016/j.ijimpeng.2008.02.003. URL: https://linkinghub.elsevier.com/retrieve/pii/S0734743X08000845 (visited on 02/10/2025).

[14] A. Evstifeev et al. “Experimental and theoretical analysis of solid particle erosion of a steel compressor blade based on incubation time concept”. en. In: *Engineering Failure Analysis* 87 (May 2018), pp. 15–21. ISSN: 13506307. DOI: 10.1016/j.engfailanal.2018.01.006. URL: https://linkinghub.elsevier.com/retrieve/pii/S1350630717306477 (visited on 02/12/2025).

[15] I. Finnie. “Some observations on the erosion of ductile metals”. en. In: *Wear* 19.1 (Jan. 1972), pp. 81–90. ISSN: 00431648. DOI: 10.1016/0043-1648(72)90444-9. URL: https://linkinghub.elsevier.com/retrieve/pii/0043164872904449 (visited on 02/13/2025).

[16] Manish Roy, B. Vishwanathan, and G. Sundararajan. “The solid particle erosion of polymer matrix composites”. en. In: *Wear* 171.1-2 (Jan. 1994), pp. 149–161. ISSN: 00431648. DOI: 10.1016/0043-1648(94)90358-1. URL: https://linkinghub.elsevier.com/retrieve/pii/0043164894903581 (visited on 02/13/2025).

[17] A Hager et al. “Study of erosion wear of advanced polymer composites”. In: (1995), p. 155–62.

[18] Y. Fouad, M. El-Meniawi, and A. Afifi. “Erosion behaviour of epoxy based unidirectionl (GFRP) composite materials”. en. In: *Alexandria Engineering Journal* 50.1 (Mar. 2011), pp. 29–34. ISSN: 11100168. DOI: 10.1016/j.aej.2011.01.005. URL: https://linkinghub.elsevier.com/retrieve/pii/S1110016811000135 (visited on 03/10/2025).

[19] Siddhartha and Renu Bisht. “A modified approach for better prediction of erosion wear of materials: Redefining the paradigms”. en. In: *Materials & Design* 47 (May 2013), pp. 395–407. ISSN: 02613069. DOI: 10.1016/j.matdes.2012.11.037. URL: https://linkinghub.elsevier.com/retrieve/pii/S0261306912007959 (visited on 02/13/2025).

[20] G. Sundararajan, M. Roy, and B. Venkataraman. “Erosion efficiency-a new parameter to characterize the dominant erosion micromechanism”. en. In: *Wear* 140.2 (Nov. 1990), pp. 369–381. ISSN: 00431648. DOI: 10.1016/0043-1648(90)90096-S. URL: https://linkinghub.elsevier.com/retrieve/pii/004316489090096S (visited on 02/13/2025).

[21] Keldon Anderson, Soroor Karimi, and Siamack Shirazi. "Erosion testing and modeling of several non-metallic materials". en. In: *Wear* 477 (July 2021), p. 203811. ISSN: 00431648. DOI: 10.1016/j.wear.2021.203811. URL: https://linkinghub.elsevier.com/retrieve/pii/S0043164821002003 (visited on 02/25/2025).

[22] Bharat Singh Chahar and Ananat Krishna Pun. "EROSION WEAR OF DUCTILE MATERIALS: A REVIEW". In: (2018).

[23] JC Arnold and IM Hutchings. "The erosive wear of elastomers". In: Journal of Natural Rubber Research (1991).

[24] Yuvaraj Natarajan et al. "Abrasive Water Jet Machining process: A state of art of review". en. In: *Journal of Manufacturing Processes* 49 (Jan. 2020), pp. 271–322. ISSN: 15266125. DOI: 10.1016/j.jmapro.2019.11.030. URL: https://linkinghub.elsevier.com/retrieve/pii/S1526612519304219 (visited on 02/27/2025).

[25] U.S Tewari et al. "Solid particle erosion of carbon fibre– and glass fibre–epoxy composites". en. In: *Composites Science and Technology* 63.3-4 (Feb. 2003), pp. 549–557. ISSN: 02663538. DOI: 10.1016/S0266-3538(02)00210-5. URL: https://linkinghub.elsevier.com/retrieve/pii/S0266353802002105 (visited on 02/14/2025).

[26] N. Miyazaki and T. Hamao. "Effect of Interfacial Strength on Erosion Behavior of FRPs". en. In: *Journal of Composite Materials* 30.1 (Jan. 1996), pp. 35–50. ISSN: 0021-9983, 1530-793X. DOI: 10.1177/002199839603000103. URL: https://journals.sagepub.com/doi/10.1177/002199839603000103 (visited on 02/14/2025).

[27] N.-M Barkoula and J Karger-Kocsis. "Effects of fibre content and relative fibre-orientation on the solid particle erosion of GF/PP composites". en. In: *Wear* 252.1-2 (Jan. 2002), pp. 80–87. ISSN: 00431648. DOI: 10.1016/S0043-1648(01)00855-9. URL: https://linkinghub.elsevier.com/retrieve/pii/S0043164801008559 (visited on 02/25/2025).

[28] Xianqiang Pei and Klaus Friedrich. "Erosive wear properties of unidirectional carbon fiber reinforced PEEK composites". en. In: *Tribology International* 55 (Nov. 2012), pp. 135–140. ISSN: 0301679X. DOI: 10.1016/j.triboint.2012.05.020. URL: https://linkinghub.elsevier.com/retrieve/pii/S0301679X12001739 (visited on 02/25/2025).

[29] Pedro P. Camanho et al. "Prediction of in situ strengths and matrix cracking in composites under transverse tension and in-plane shear". en. In: *Composites Part A: Applied Science and Manufacturing* 37.2 (Feb. 2006), pp. 165–176. ISSN: 1359835X. DOI: 10.1016/j.compositesa.2005.04.023. URL: https://linkinghub.elsevier.com/retrieve/pii/S1359835X05002526 (visited on 02/17/2025).

[30] G. Catalanotti, P.P. Camanho, and A.T. Marques. "Three-dimensional failure criteria for fiber-reinforced laminates". en. In: *Composite Structures* 95 (Jan. 2013), pp. 63–79. ISSN: 02638223. DOI: 10.1016/j.compstruct.2012.07.016. URL: https://linkinghub.elsevier.com/retrieve/pii/S0263822312003443 (visited on 02/17/2025).

[31] A Puck. "Failure analysis of FRP laminates by means of physically based phenomenological models". In: *Composites Science and Technology* 58.7 (July 1998), pp. 1045–1067. ISSN: 02663538. DOI: 10.1016/S0266-3538(96)00140-6. URL: https://linkinghub.elsevier.com/retrieve/pii/S0266353896001406 (visited on 02/17/2025).

[32] C Herakovich. "Damage evolution in [±45]s laminates with fiber rotation". In: *Composites Science and Technology* 60.15 (Nov. 2000), pp. 2781–2789. ISSN: 02663538. DOI: 10.1016/S0266-3538(00)00091-9. URL: https://linkinghub.elsevier.com/retrieve/pii/S0266353800000919 (visited on 02/17/2025).

[33] P Ladeveze and E Ledantec. "Damage modelling of the elementary ply for laminated composites". en. In: *Composites Science and Technology* 43.3 (1992), pp. 257–267. ISSN: 02663538. DOI: 10.1016/0266-3538(92)90097-M. URL: https://linkinghub.elsevier.com/retrieve/pii/026635389290097M (visited on 02/17/2025).

[34] G. L. M. Rocha Coelho. "Modelling of damage and failure of thermoplas tic matrix composite laminates". PhD thesis. Universidade do porto, Porto, Portugal, Oct. 2023.

[35] P. Linde et al. "Modelling and simulation of fibre metal laminates". In: ABAQUS Users' Conference (2004).

[36] Harlal Singh Mali. "A Micromechanical Unit Cell Model of 2 × 2 Twill Woven Fabric Textile Composite for Multi Scale Analysis". In: (2014).

[37] Adrien Sapet. "D´eveloppement d'un banc d'essai et de son image num´erique pour comprendre et am´eliorer la r´esistance 'a l'´erosion des pi'eces a´eronautiques". PhD thesis. ISAE Supaero.